

Subaru Prime Focus Camera – Suprime-Cam –

Satoshi MIYAZAKI^{1,2}, Yutaka KOMIYAMA³, Maki SEKIGUCHI⁴, Sadanori OKAMURA^{5,6},
Mamoru DOI^{7,6}, Hisanori FURUSAWA^{5,3}, Masaru HAMABE⁸, Katsumi IMI^{3,*},
Masahiko KIMURA^{4,†}, Fumiaki NAKATA^{5,1}, Norio OKADA¹, Masami OUCHI⁵,
Kazuhiro SHIMASAKU^{5,6}, Masafumi YAGI¹, and Naoki YASUDA^{1,2}

¹*National Astronomical Observatory, Mitaka, Tokyo 181-8588*

²*The Graduate University for Advanced Studies (Sokendai)*

³*National Astronomical Observatory of Japan, Hilo, Hawaii 96720, U.S.A.*

⁴*Institute for Cosmic Ray Research, The University of Tokyo, Kashiwa, Chiba 277-8582*

⁵*Department of Astronomy, The University of Tokyo, Bunkyo, Tokyo 113-8654*

⁶*Research Center for the Early Universe, The University of Tokyo, Tokyo 113-8654*

⁷*Institute of Astronomy, The University of Tokyo, Mitaka, Tokyo 181-0015*

⁸*Department of Mathematical and Physical Sciences, Japan Women's University, Bunkyo, Tokyo 112-8681*

^{*}*Present address: Communication Network Center (Tsu-den), Mitsubishi Electric, Amagasaki, Hyogo 661-8661*

[†]*Present address: Department of Astronomy, Kyoto University, Sakyo, Kyoto 606-8502*

satoshi@naoj.org

(Received July 9, 2002; accepted October 25, 2002)

Abstract

We have built an 80-mega pixels (10240×8192) mosaic CCD camera, called Suprime-Cam, for the wide-field prime focus of the 8.2 m Subaru telescope. Suprime-Cam covers a field of view 34'×27', a unique facility among the the 8-10 m class telescopes, with a resolution of 0."202 per pixel. The focal plane consists of ten high-resistivity 2k×4k CCDs developed by MIT Lincoln Laboratory, which are cooled by a large stirling-cycle cooler. The CCD readout electronics was designed to be scalable, which allows the multiple read-out of tens of CCDs. It takes 50 seconds to readout entire arrays. We designed a filter-exchange mechanism of the jukebox type that can hold up to ten large filters (205×170×15 mm³). The wide-field corrector is basically a three-lens Wynne-type, but has a new type of atmospheric dispersion corrector. The corrector provides a flat focal plane and an un-vignetted field of view of 30' in diameter. The achieved co-planarity of the focal array mosaic is smaller than 30 μm peak-to-peak, which realizes mostly the seeing limited image over the entire field. The median seeing in the I_c -band, measured over one year and a half, is 0."61. The PSF anisotropy in Suprime-Cam images, estimated by stellar ellipticities, is about 2% under this median seeing condition. At the time of commissioning, Suprime-Cam had the largest survey speed, which is defined as the field of view multiplied by the primary mirror area of the telescope, among those cameras built for sub-arcsecond

imaging.

Key words: Instrumentation: detectors, techniques: image processing, telescopes

1. Introduction

In the mid 1980's during a concept study of Subaru telescope, a working group on wide-field astronomy stated that the minimum required field of view is $0^\circ.5$ in diameter. This conclusion was based on the statistics of the apparent size of various objects. The recommended field of view was realized at the prime focus. The wide-field prime focus became a unique feature of Subaru among very large telescopes, such as Keck and VLT. We designed and built a CCD mosaic camera for the prime focus: **Subaru Prime Focus Camera**, Suprime-Cam. This paper presents the hardware and performance of Suprime-Cam.

In order to take full advantage of the good image quality on Mauna Kea, we set the goal of Suprime-cam as the realization of natural seeing limited images over the entire field of view. We assumed the best natural seeing to be $0.''4$ based on the achievements by HRCam (McClure et al. 1989) and a median value of $0.''7$ - $0.''8$. One of the most critical components regarding the image quality of Suprime-Cam is the wide field corrector for the prime focus. Takeshi (2000) worked out a novel design of the corrector to realize compact size while maintaining image quality. At a telescope elevation angle of 90° the diameter encircling the 80 % energy of a point source is $0''.15$ at the field center for the design wavelength (546.1 nm) and less than $0.''3$ for the entire wavelength region at any position in the field of view. The co-planarity and stability of the cold focal plane is another key for image quality. The fast F-ratio of 1.86 of the prime focus requires a tight tolerance. We have developed a new method of mounting CCDs (subsection 2.3) and a mechanically stable frame (subsection 2.8).

The observing efficiency is also an important design goal. Because of the very fast F-ratio, the exposure times for broad-band filters are relatively short. In particular, they are on the order of a few to several minutes at longer wavelengths where the sky brightness is high. The overhead due to CCD readout should be minimized. CCDs that can be clocked fast combined with high speed readout electronics are crucial for this purpose. All of the mechanics, including a shutter and a filter exchanger, must be highly reliable, since the camera is hard to reach once installed on the telescope. Accordingly, how to hold and how to exchange as many large (205×107 mm) filters as possible is also a critical issue related to the observing efficiency.

WFPC2 on board the Hubble Space Telescope has indeed had revolutionary impacts on observational astronomy. This is due to the superb image quality ($\leq 0.''1$) over the modest field of view, which cannot be obtained from the ground in the visible wavelength, even if one employs adaptive optics. Computations and image simulations made in a design study, however, indicated that for a given exposure time Suprime-Cam could reach similar or slightly deeper limiting magnitude, though with a poorer spatial resolution, if all the design specifications were

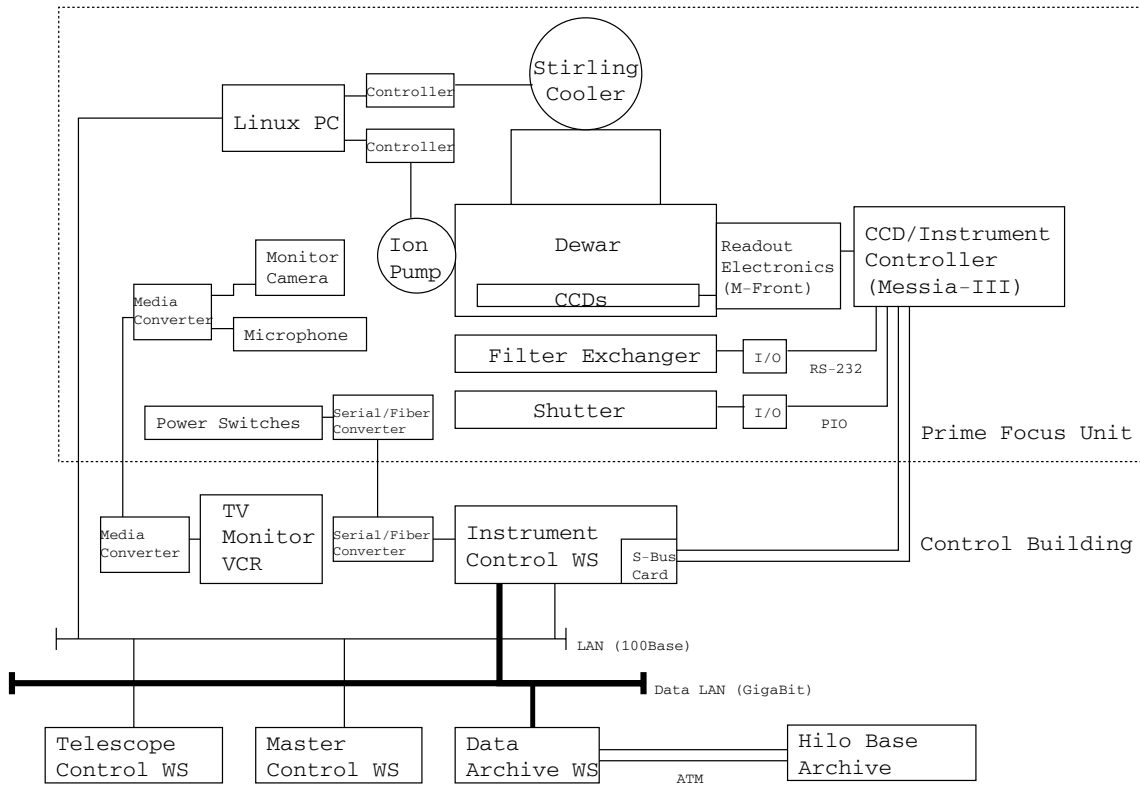


Fig. 1. Hardware block diagram of Suprime-Cam.

met. This was encouraging and our goal was the realization of stable sub-arcsec image, as good as $0.''4$ in extreme cases, over a more than 100-times wider field of view than WFPC2. Such sub-arcsec imaging with Suprime-Cam will give many unique opportunities to researches in various fields where the spatial resolution attainable only from space telescopes is not a critical factor.

The plan of this paper is as follows. In section 2 we describe in detail the mechanical design of various components of Suprime-Cam with the intention to include important information useful to similar development efforts. In section 3 we describe the performance verification processes and achieved performance. Conclusions are given in section 4. Appendix describes the effect of atmospheric differential refraction.

2. Hardware of Suprime-Cam

2.1. Overview

A hardware block diagram of the camera is shown in figure 1. The main science imagers, CCDs, are controlled by electronics called M-front and Messia-III. A cryogenic system, consisting of a dewar, a mechanical cooler and an ion pump, keep the temperature of the CCD at -110°C so that the dark current of CCDs becomes negligible for a period on the order of one hour. A dedicated Linux-PC controls the cooler and the pump by monitoring the temperature

of the dewar. A filter exchanger and a shutter are major mechanical components of the camera, and are controlled through the instrument controller on board Messia-III. It is connected to an instrument control workstation (WS) located in a control building via 500 m long optical fiber lines. A small CCD camera and microphones are installed inside the frame to monitor the motion of the mechanical parts, and those audio-visual signals are multiplexed and transmitted to the building via a single fiber line. There are several other WS's in the control room, including a master control WS, a dedicated WS to control the telescope and a WS for the data archive. The observing commands are issued from the master control WS to others. In the following, we present descriptions of the hardware components of Suprime-Cam.

2.2. CCD

Although the physical size of the focal plane is relatively small (ϕ 150 mm), thanks to the fast F-ratio, there was no CCD available with which the entire field of view can be covered. Therefore, mosaicing of several devices is inevitable. At the design phase of Suprime-Cam, the largest device commercially available was the Tektronix (later SITe) Tk2048E, which has a $2k \times 2k$ array of $24 \mu\text{m}$ pixel. The Tk2048E used to be the most appropriate device for wide field imaging, and has been employed by many cameras, such as the SDSS photometric camera (Gunn et al. 1998). The Tk2048E, however, has the following disadvantages when used for Suprime-Cam: (1) the pixel size results in a coarse sampling of $0.''32$, which is not sufficient for the best seeing at Mauna Kea ($\sim 0.''4$), (2) the I/O bonding pads surrounding the device cause the inter-device gap to be larger, which is irrelevant for the relatively narrow physical size of the Suprime-Cam's focal plane, (3) the device must be read very slowly, for 3 to 4 minutes, to avoid smearing through losses in the charge transfer, which reduces the observing efficiency significantly unless the TDI mode is adopted.

In the meantime, a back-illuminated 4096×2048 array of $15 \mu\text{m}$ square pixels was becoming available. We then decided to employ a three side buttable device of that format whose pads are located on a single short side so that gaps along the other three sides are minimized. There are three vendors which supplied that type of CCD: MIT Lincoln Laboratory (MIT/LL) (Burke et al. 1998), E2V (the former EEV) (Oates & Jorden 1998), and SITe (Blouke et al. 1998). The SITe's ST002A has a similar quantum efficiency (QE) as the Tk2048E and cannot be read out fast, either. The QE of the MIT/LL's CCID-20 is optimized for longer wavelength, whereas the E2V's CCD42-80 has a high QE in shorter wavelengths as shown in figure 2. These two devices can be clocked faster than ST002A and can be read out in less than 1 minute while keeping the readout noise below ~ 5 electrons. Because we had a high priority on the red response, we had adopted CCID-20 for Suprime-Cam. A sufficient number of CCID-20's, however, were not available before the scheduled first light in early 1999. We therefore mixed several ST002A's to the mosaic in the beginning and later made a full replacement of those to CCID-20's in 2000 April.

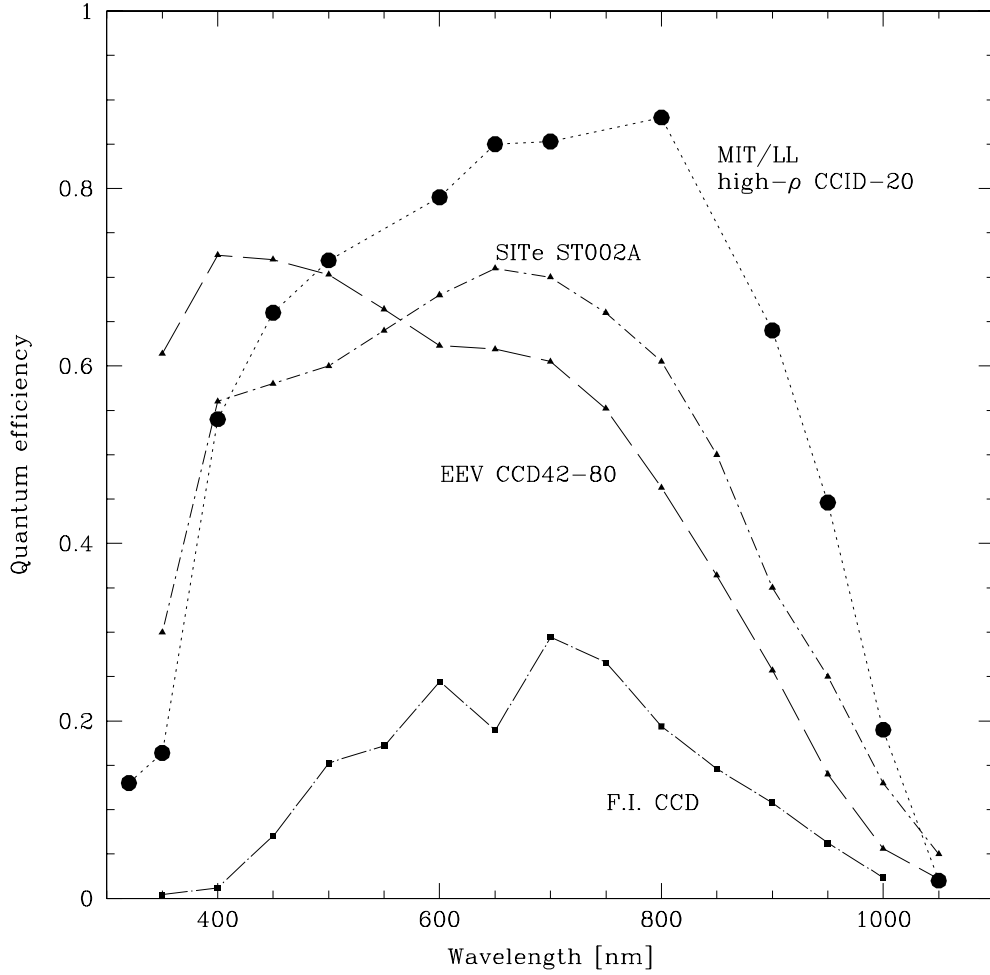


Fig. 2. Quantum efficiency of CCDs measured at NAOJ/ATC detector laboratory.

The development of CCID-20 was funded by a consortium led by University of Hawaii. The device was initially fabricated on an ordinary silicon wafer, but was later fabricated on high-resistivity (ρ) silicon (2-3 k Ω cm). The advantage of the high- ρ type CCD is its thicker depletion layer, which improves the QE, especially at longer wavelengths by 15% to 20% compared with the QE of ordinary type. Another advantage of the high- ρ CCD is the absence of interference fringing which occurs due to multiple reflections internal to the device. The fringing used be a real burden of the backside-illuminated CCDs at longer wavelengths. The CCID-20 is the first high- ρ device available for a community of optical astronomy. MIT/LL claims that the thickness of the depletion layer is about 40 μ m. All of the CCDs installed in the camera are of the high- ρ type with double layers of HfO₂/SiO₂ AR coating, except for one that is built on the standard- ρ silicon with a TiO₂/Al₂O₃ coating. The flatness of the device on the specification sheet given by the consortium was 20 μ m, but the actual flatness is \sim 10 μ m on most of the

Table 1. CCD related parameters of Suprime-Cam

C.F.	Read noise	Pixel rate	saturation level	dark current (-110°C)
$2.6 \pm 0.1 \text{ e}^-/\text{ADU}$	$5\text{-}10 \text{ e}^-$	$6 \mu\text{s}$	92000 e^-	$2\text{-}3 \text{ e}^-/\text{hr}$

devices (see figure 5). Without this level of intrinsic flatness, we could not achieve a flat focal plane, as is shown in the next section.

Table 1 presents the CCD-related characteristics of the Suprime-Cam measured. The Conversion Factor (C.F.) were measured at a laboratory using MnK_{α} X-rays of ^{55}Fe , and all the others were measured in the telescope environment. The saturation level in the table is the point where the response deviates by 0.5% from the linear response. The value is limited by the design of the current electronics, and is slightly lower than the value of 100000 e^- reported by Lick observatory (Wei & Stover 1998). Since the focal-plane arrays are maintained at -110°C , the dark current is completely negligible for the typical 5-20 min exposure. We adopted a rather conventional pixel rate of $6 \mu\text{s}$, and it takes 50 s to read out the entire array. The read noise is slightly higher than the best record which we obtained in the laboratory ($2\text{-}3 \text{ e}^-$). Although we have not fully identified the noise sources, we felt that the cooler and the associated power electronics might be the dominant causes. The sky shot noise, however, usually dominates, and exceeds ~ 50 electrons, even if one uses an extremely narrow band filter of $\Delta\lambda = 7 \text{ nm}$ with a reasonable length of exposure time (15 min).

The bias level can be estimated from the over-scan-region that is created by clocking more times than the actual number of pixels, and no charge is dumped into the sense node of the output amplifier. The variation of the bias level monitored over about one year is no more than 1% around the mean thanks to the stable operating temperature.

A flat-field frame is usually created by stacking tens of blank sky images. Below 450 nm (i.e., in the B band), the non-uniformity of the QE of the CCD becomes apparent. The non-uniformity, called *brick wall pattern*, is an imprint of the laser stepping pattern during the backside passivation process. The degree of non-uniformity badly depends on the device temperature. The variation of the non-uniformity, defined as $(\text{max} - \text{min})/\text{mean}$, is about $-0.5\%/\text{deg}$ at -110°C (Wei & Stover 1998). Therefore, the change is little if the temperature control system functions normally to realize $\Delta T < \pm 0.3 \text{ deg}$. The scattering of QE averaged over each device among the nine high- ρ CCDs is not broad, 3-4% around the mean. The one standard- ρ device installed has about 25-30% less QE over the entire sensitive wavelength than others, since the AR coating of this particular device was not fully optimized.

The interference fringing is actually not visible on high- ρ CCDs up to the I_c band, whereas a slight sign of fringing sometimes appears on the z' band images. This is, however, quite small (about 0.2 % at most) compared with sky shot noise, and disappears without any subtraction of a fringe frame after dithered exposures are stacked.

2.3. CCD Mounting

2.3.1. The requirements

The prime-focus corrector is designed to give a flat focal plane where the focal depth is simply estimated by the pixel size ($15\ \mu\text{m}$) multiplied by the F-ratio (1.86), $\sim \pm 30\ \mu\text{m}$ (see subsection 2.9). In order to realize the seeing-limited image, the CCD surface, i.e., the imaging area of the CCDs, over the entire field of view should be located within the focal depth. We set the specification of the co-planarity at half of the focal depth ($= \pm 15\ \mu\text{m}$) to leave a margin for any mechanical errors in the flatness of the large cold plate. Another design requirement is the easiness of installation and un-installation of CCDs. This is important, since the best-quality high- ρ devices had been hard to obtain in bulk in time during our development phase of the camera. We actually had to swap the CCDs several times for upgrades. Thus we have developed a new scheme for mounting CCDs to meet these requirements.

2.3.2. Compensating tilt of CCDs

The CCD surface is usually tilted with respect to the bottom surface of the package. Thus, the height of the CCD surface from the bottom surface is different over a CCD chip. The height difference sometimes exceeds $100\ \mu\text{m}$. A conventional method to compensate for the tilt is to insert a metal shim block between a CCD and the cold plate (Wolfe et al. 1998). This requires a precise relative alignment of the CCD and the blocks. Furthermore, since the heat path between the CCD and the cold plate is limited to the narrow channel through the metal block, which results in a longer cooling time, additional cold straps are necessary to make the heat path wide. We felt that these could make the installation process overwhelming. We therefore developed a new method of CCD mounting. A detailed description of the method was first given in Nakata et al. (2000) during the course of the development. Here, we show the final results as well as a summary of the procedure.

We compensated for the tilt by employing a buffer block between a CCD and the cold plate, as shown in figure 3. The buffer block is epoxied to the CCD with thin metal foils of the appropriate height inserted. We chose the same material for the buffer block as the CCD package, aluminum-nitride (AlN) ceramic, while considering the effect of thermal expansion. The buffer block also has alignment pins, which are epoxied with 3M glue (2216 B/A Gray). The diameter of the alignment pins was originally made slightly larger than the diameter of the holes on the cold plate. After being epoxied to the buffer block, each alignment pin was precisely machined to make its center coincident with the center of the hole to which it should fit. The diameter of the alignment pin is made smaller in this process than that of the hole by $\sim 30\ \mu\text{m}$ so as to guarantee the smooth insertion. The pins have screw-type threads that can be used to fix the buffer block to the cold plate using nuts and belleville springs from the opposite side.

We designed and built a special working bench to do the job, as shown in figure 4.

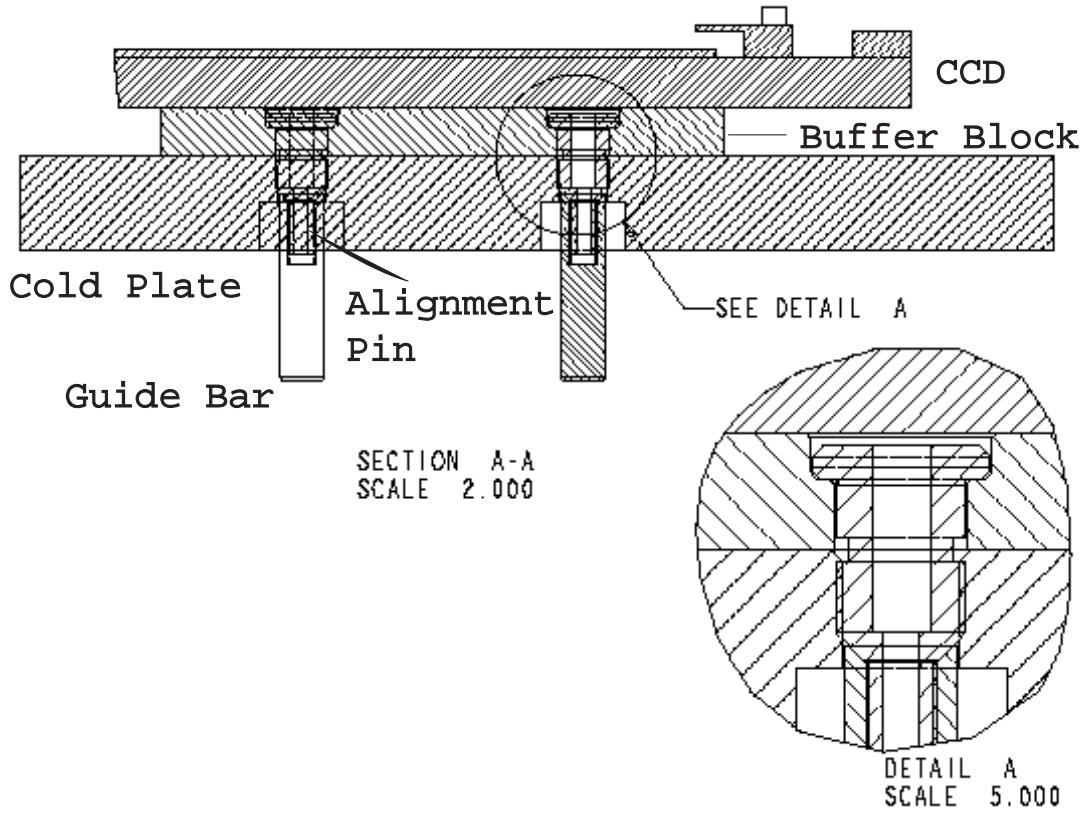


Fig. 3. Cross sectional view of a CCD with a buffer block mounted on the cold plate

The bench was fixed on an X-Y stage, which equipped with a microscope to measure the X-Y position, and a high precision laser-displacement meter (Keyence LC-2430) to measure the height of the imaging area of the CCD. First, we measured the surface profile of a CCD without the foils. It turned out that the heights of evenly spaced 3×3 points were sufficient to characterize the CCD surface, because a height variation of smaller scale is negligible. Some devices have a tilt larger than $100 \mu\text{m}$ from one corner to the diagonally opposite corner.

We then calculated the appropriate height of thin metal foils to minimize the height variation from the fiducial plane. The foils were inserted at the four corners of the buffer block (figure 4, top) and we measured the surface profile again. If necessary, additional foils were inserted. When the height variation became small enough (typically $10 \mu\text{m}$ p-p), the 3M glue was filled between the CCD and the block. The CCD was pushed down to secure the contact with the metal foils by a hook using dips on the sides of the CCD package (figure 4, bottom). When epoxying the block to the CCD, the horizontal (X-Y) alignment was realized by pushing the CCD with screws and plungers attached to the side of the working bench with the position being monitored by the microscope. After the CCD is fixed to the block, we measured the heights to see the difference before and after the cure. The difference was always as small as $\sim 2 \mu\text{m}$.

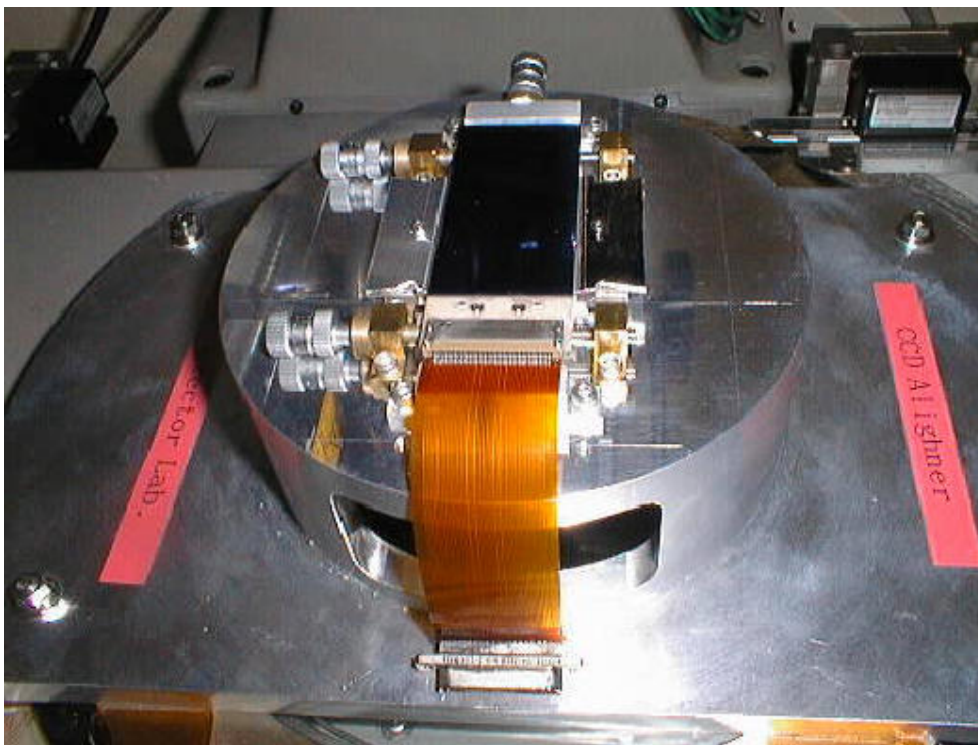
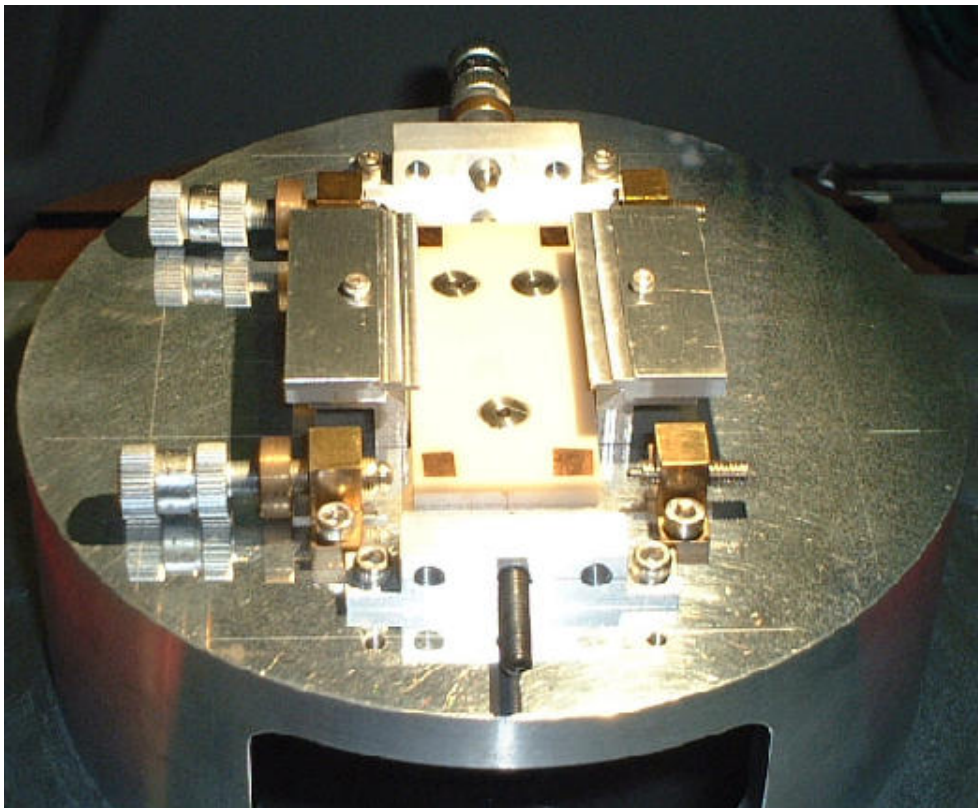


Fig. 4. Four pieces of thin metal foils are put at the four corners of the buffer block (top). A CCD package is pushed down by a hook on the side of the alignment bench to be glued to the buffer block (bottom).

Finally, we installed the CCDs with the block to the cold plate. The cold plate was made of AlN manufactured and precisely machined by Mitsui Mining & Smelting. The X-Y location of the CCDs on the cold plate was determined by the alignment pins attached to the buffer block and the holes on the cold plate. When we inserted the pins to the holes of the cold plate, we attached cylindrical bars with a tapped hole on top to the alignment pins, and the bars were used for a guide to avoid butting the fragile CCDs (figure 3). After insertion, the bars were removed and the nuts and springs were used to fix the CCDs. The use of guide bars is one of the unique features to realize the easy replacement of CCDs for a future upgrade.

Figure 5 shows the measured height variation of the final mosaic configuration. We can see that the heights of the CCD surfaces satisfy the requirement. The distance to any point from the fiducial plane is less than $12.7\ \mu\text{m}$. We notice that the planarity of one of the CCD is significantly worse than those of other CCDs; CCD5 in the figure is apparently *twisted*. It records the largest deviation from the fiducial plane. The typical gap between neighboring CCDs is 1.35 mm along the short direction of CCDs and 0.81 mm along the long direction. Each CCD has a slight rotation angle on the order of 0.0027 radians, which is consistent with the allowance of the fitting ($\Delta r = 30\ \mu\text{m}$) between the alignment pins and the holes.

2.4. CCD Readout Electronics: M-Front and Messia-III

The CCD readout electronics system was originally developed in collaboration with National Astronomical Observatory and the University of Tokyo. A block diagram of the electronics is shown in figure 6. A DSP-based programmable clock generator integrated with instrument controllers is called *Messia-III* (Sekiguchi et al. 1998). The analog part of the CCD electronics is called *M-Front*, and its design is based on the electronics system of the SDSS photometric camera (Gunn et al. 1998). *Messia-III* sends CCD clocks to *M-Front* and monitors the clock voltage through the I/O port. *M-Front* sends 16-bit digital data back to the frame memory on *Messia-III*. We present a brief description of the electronics system here.

Each CCD is connected to a dedicated small Flexible Printed Circuit board, called *clkamp* (figure 7), which has analog-switch based clock line drivers and two pre-amplifiers for the CCD output. *Clkamp*'s are installed in the vacuum dewar to minimize the wiring length between the CCD and the pre-amplifier. Thanks to the existence of the circuits, the CCD has a low risk of electrostatic discharge damage once installed in the dewar. One drawback of the configuration is that circuit adjustments become troublesome tasks. Another drawback is an increase of the ungassing of these components, which is noticeable from the longer pumping time required. However, once the dewar is pumped down and the CCDs are cooled, the vacuum can be maintained by the ion pump. We therefore think that the ungassing is practically harmless.

M-Front adopts conventional dual-slope correlated double sampling (CDS), whose RC constant is set at $1\ \mu\text{s}$. Analogic's ADC4235 (16 bit 500 kHz) is employed as an Analog to Digital Converter (ADC). The time needed to handle one pixel amounts to $6\ \mu\text{s}$, which includes

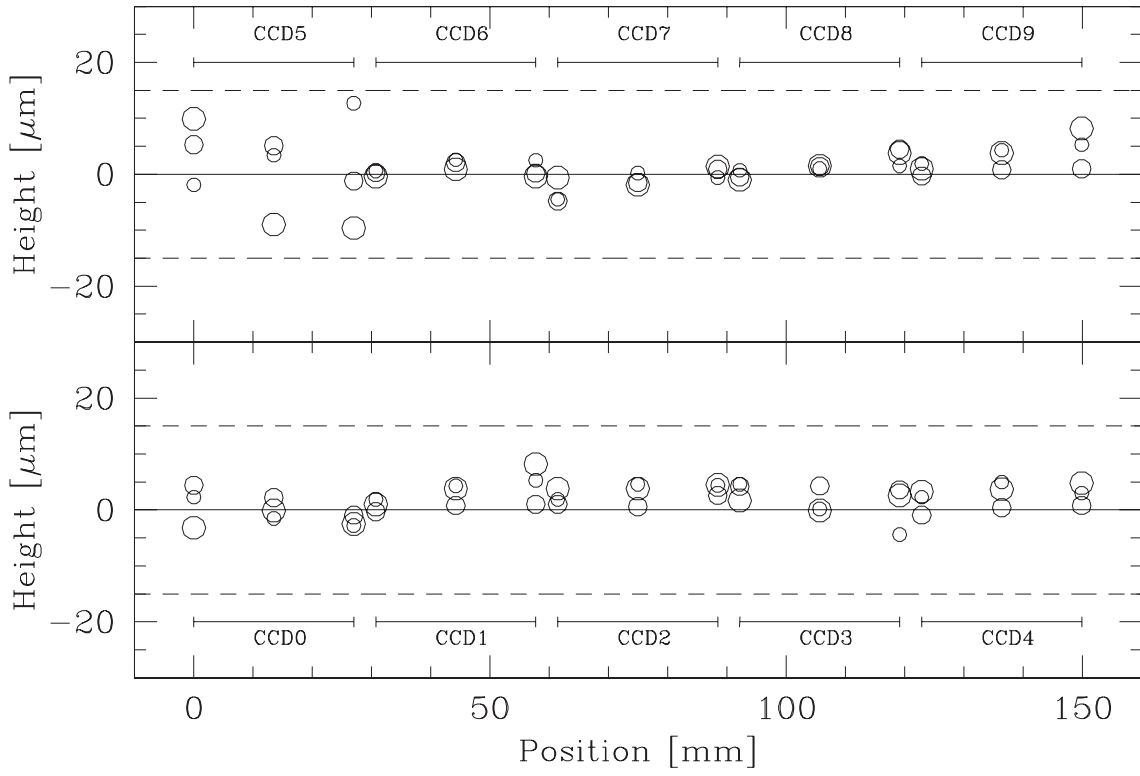


Fig. 5. Height variation of CCD surfaces after compensation. The horizontal axis shows a distance along the short direction (X-direction) of the CCD and three points along the long direction (Y-direction) (the center and ± 26 mm) are measured at each X position. The size of the symbol in the figure indicates the Y position; the symbol becomes smaller as Y increases. The solid lines indicate the fiducial plane and the dashed lines correspond to our design goal ($\pm 15 \mu\text{m}$).

serial clocking, the integration time of the CDS and the dead time to wait for a settlement of the analog switch used in the CDS. The total time to readout the CCID20 ($4\text{k} \times 2\text{k}$ pixels) is thus about 50 seconds. Figure 8 shows the output of the *clkamp* ($\times 10$ of CCD output) and the output of the CDS fed to the ADC.

The bias voltages for CCDs are generated by EEPROM-based DAC chips. M-Front has two additional boards: *REG*, which has power regulators, and *RCV* which receives/sends differential signals from/to Messia-III. The size of all the boards is EuroCard 3U ($10 \text{ cm} \times 16 \text{ cm}$), except for the ADC board, which has almost half of the other boards. Two ADC boards are piggyback mounted on the bias board. All of the EuroCards are interconnected via 96 pin DIN connectors.

2.5. Dewar and the Cooling System

2.5.1. Mechanical design

Figure 9 shows an exploded view of the vacuum dewar of the Suprime-Cam. CCDs are attached to an AlN cold plate whose size is $224 \text{ mm} \times 170 \text{ mm}$ and 10 mm in thickness. It attains $5 \mu\text{m}$ flatness on each surface and $5 \mu\text{m}$ parallelism between two surfaces, which is the

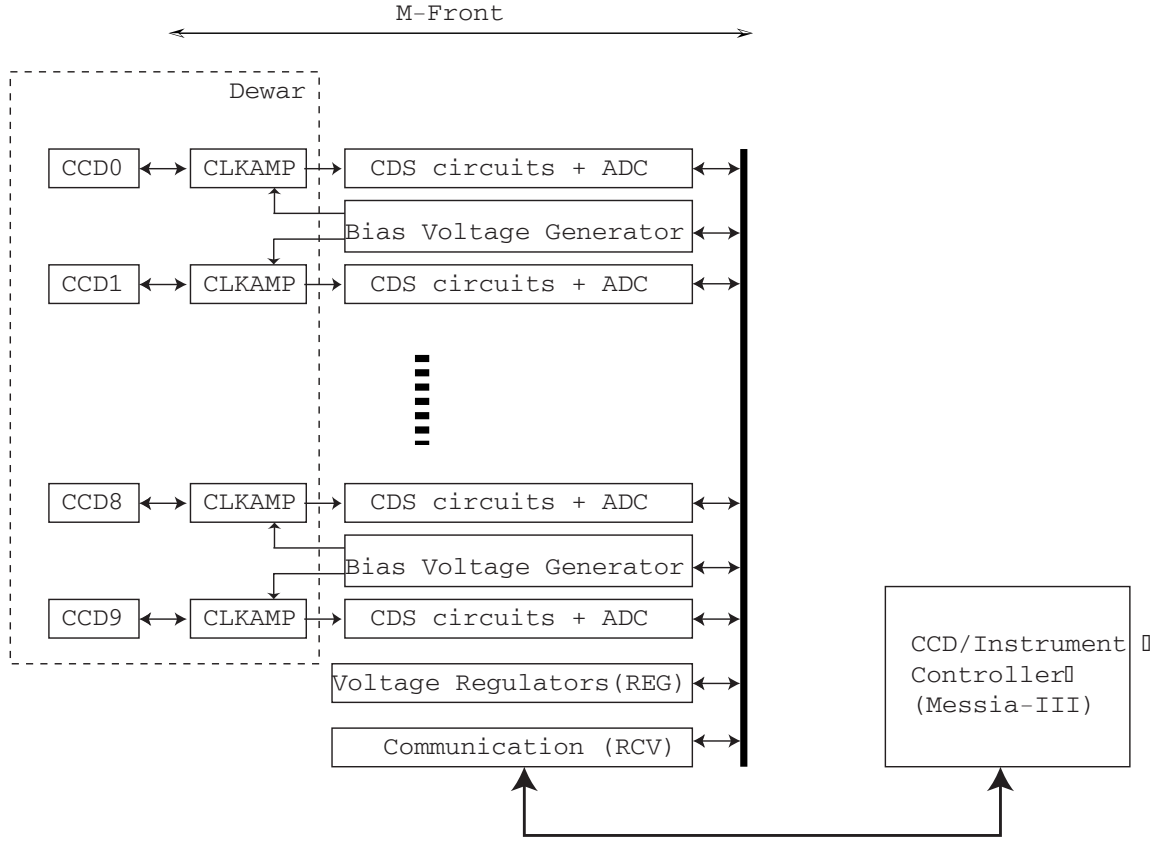


Fig. 6. Block diagram of the CCD electronics adopted for Suprime-Cam; M-Front and Messiah-III.

basis to make the mosaic of ten CCDs co-planar. Thin gold-plated radiation shields cover the plate to minimize the heat inflow.

The cold plate is supported by four polycarbonate posts (G2530; 30% glass fiber contained) with buried taps. Polycarbonate has a low thermal conductivity ($0.1-0.2 \text{ W m}^{-1} \text{ K}^{-1}$) in addition to a high Young modulus ($7-8 \times 10^4 \text{ kg cm}^{-2}$), which makes it possible to keep the cold plate isolated thermally and to hold it stably to the dewar. These posts are designed like *X-shaped*, whose side and bottom parts are trimmed so as to reduce the thermal conduction while maintaining mechanical stiffness (see figure 9).

Twelve hermetic connectors are attached to the side of the dewar for feed-through: ten for the clkamp's for the CCDs and two for auxiliary signals, such as temperature sensors. Cables from these connectors are connected to the M-Front modules attached directly to the dewar.

Anti-reflection coated fused silica (230 mm ϕ and 15 mm thickness) is employed for the entrance window of the dewar. The material properties of the fused silica are listed in table 2. The thickness of the window is determined as follows. For a circular disk of radius R and thickness t , which is supported at its circumference, the stress to the surface is maximum at the center and is calculated as

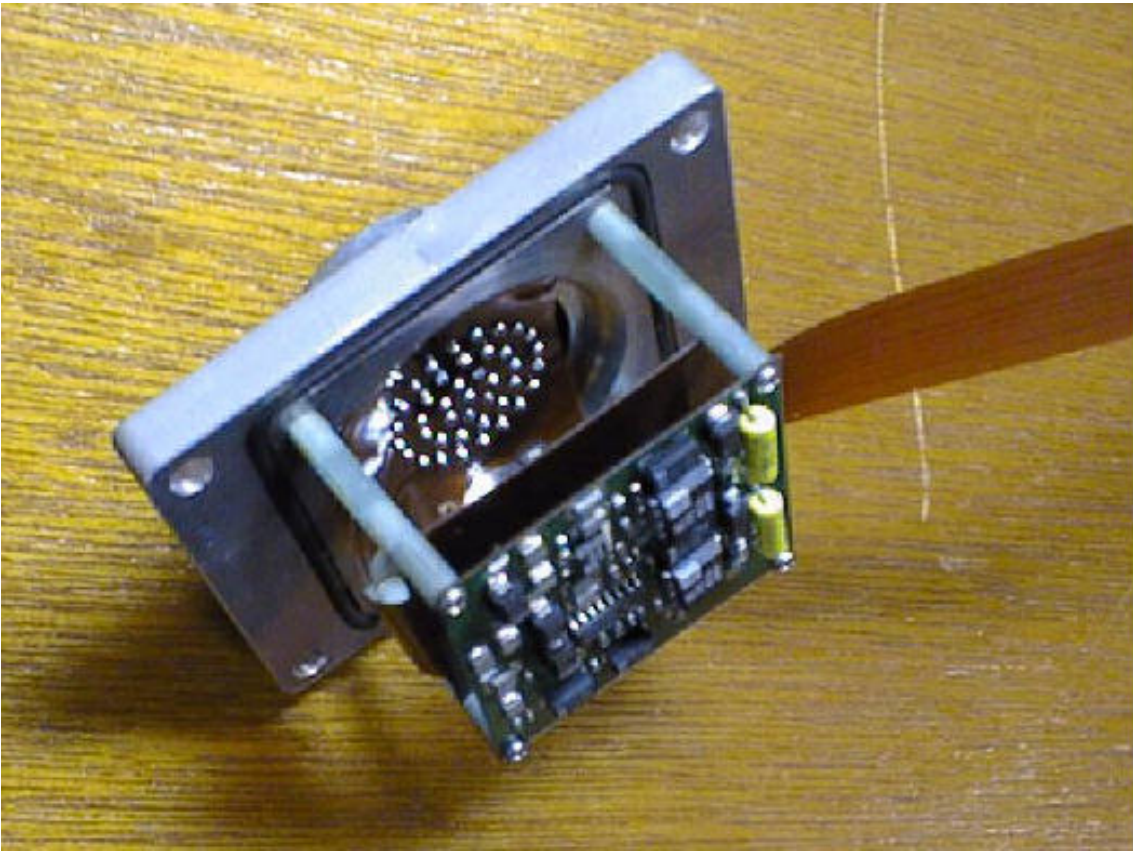


Fig. 7. Clkamp; a Flexible Printed Circuit board installed in the dewar. The board has two pre-amplifiers (this side) and analog-switch based clock line drivers (opposite side). The CCD is connected to the end of the flexible wiring shown to the right in the figure.

$$\sigma_{max} = \frac{3P(3 + \nu)}{8} \left(\frac{R}{t} \right)^2, \quad (1)$$

where P is the pressure difference between the inner and outer surfaces of the window and ν is the Poisson ratio (Lifshitz & Landau 1953). This stress must be less than the breaking strength, F_a with a safety factor of S (i.e., $\sigma_{max} < SF_a$). To prevent the window from cracking by tiny impact, it is recommended that $S > 3$. Hence, we adopt $t = 10$ mm for the window ($R = 113.2$ mm). In this condition, the bow at the window center, l , is calculated as

$$l = \frac{3P(1 - \nu)(5 + \nu)}{16E} \frac{R^4}{t^3}, \quad (2)$$

where E is Young modulus. We obtain $l = 192.1 \mu\text{m}$. We found by ray tracing that the bow introduces little optical degradation. Continuous flow of dry air is provided to the window surface to prevent water condensations during observing runs.

2.5.2. Thermal design

In order to maintain the dark current to be negligible, the temperature of the CCDs should be kept below -105°C . We set the operating temperature at -110°C while allowing for

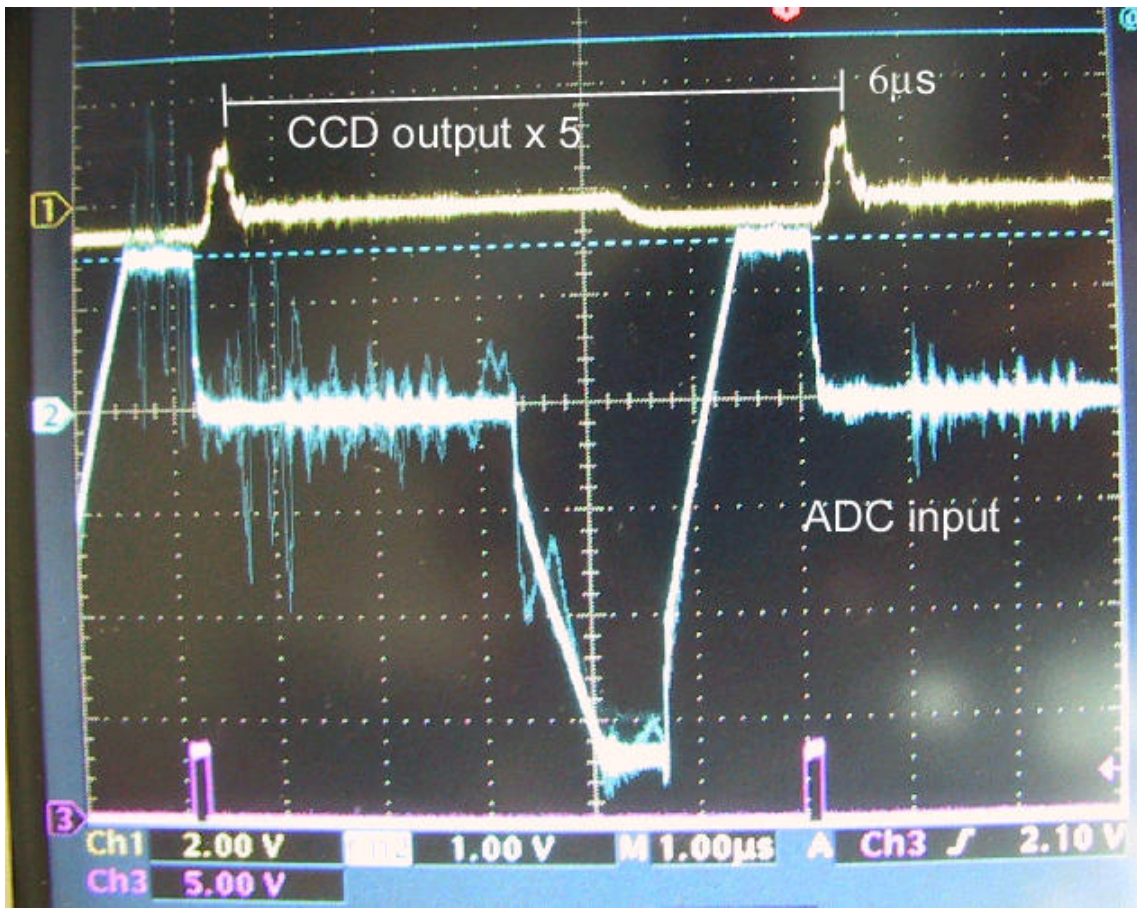


Fig. 8. Output waveform of the CCID20 and the output of the correlated double sampling of *M-Front* fed to ADC. It seems that the CCID20 can be clocked much faster because of the fast response of the signal. We, however, avoid critical setting of the timing, since we noted that the chattering that occurred at the analog switch of the CDS circuits causes an unstable output.

Table 2. Material properties of fused silica.

Breaking strength (F_a)	4.892×10^7 Pa
Young modulus (E)	6.966×10^{10} Pa
Poisson ratio (ν)	0.17

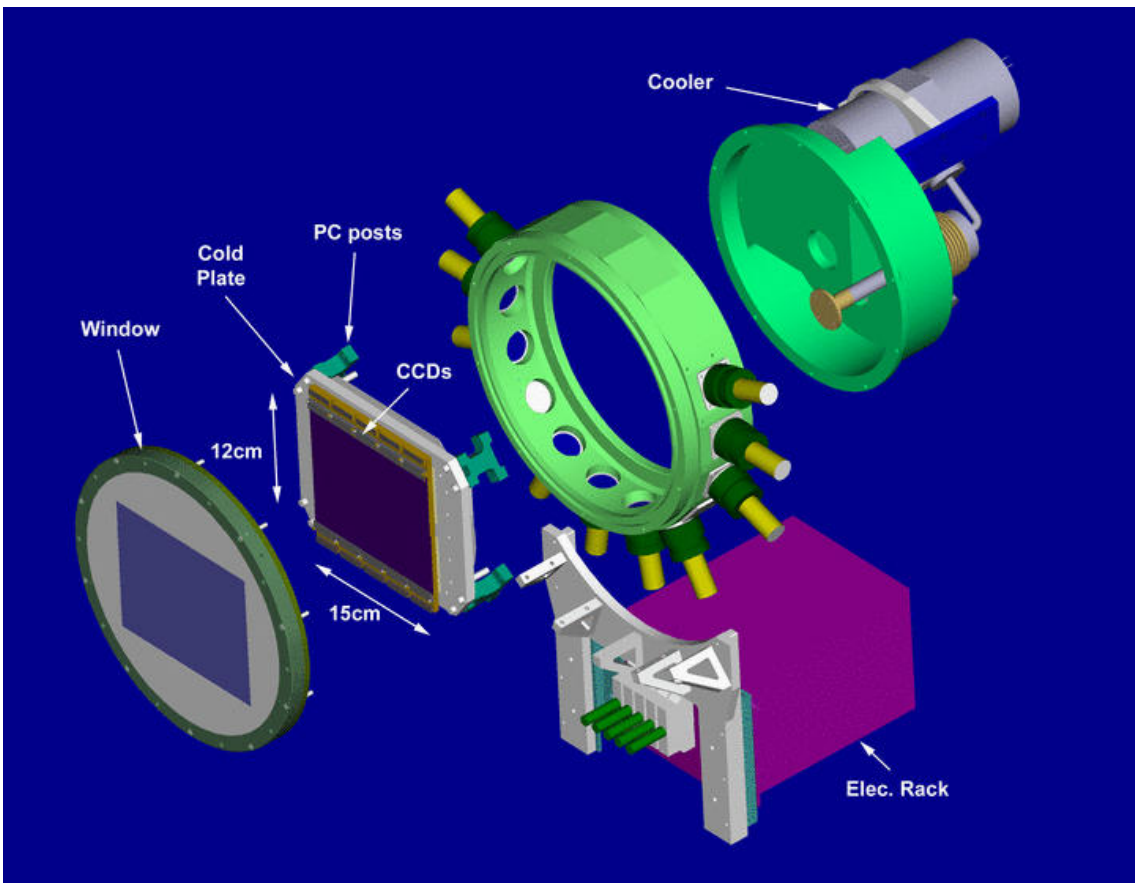


Fig. 9. Exploded view of the vacuum dewar of Suprime-Cam.

some margin. Under this condition, the dominant components of thermal inflow are the radiation from the window (a) and the wall of the dewar (b). Other components include conduction through the polycarbonate posts (c) and the wiring of electronics (d). The convection by the remaining molecules in the dewar is less than 10^{-3} W, and can be negligible if the dewar is evacuated down to 10^{-6} Torr. We give the thermal inflow of the four components, (a) – (d), above.

Thermal transfer due to the radiation from a high-temperature surface (temperature T_H with emissivity ϵ_H) to a low-temperature surface (T_L and ϵ_L) is calculated as

$$\dot{Q}_{rad} = \sigma A (T_H^4 - T_L^4) \frac{\epsilon_H \epsilon_L}{\epsilon_H + \epsilon_L - \epsilon_H \epsilon_L}, \quad (3)$$

where σ is the Stephan-Boltzmann constant (5.67×10^{-8} W m $^{-2}$ K $^{-4}$) and A is the area (Luppino & Miller 1992). The transfer due to the conduction is

$$\dot{Q}_{cond} = \frac{\bar{\kappa} A}{L} (T_H - T_L), \quad (4)$$

where $\bar{\kappa}$ is the average conductivity, A the section and L the length of the material. The total thermal inflow amounts to 7.22 W, as is given in table 3 together with the input parameters of the dewar.

Table 3. Thermal inflows to the dewar.

Component*	Amount (W)	Input Parameters ($T_H=283$ K and $T_L=163$ K are assumed.)
(a)	6.2	$\epsilon_H = 1.0$ (Window), $\epsilon_L = 0.5$ (CCD), $A = 224 \times 170 \text{ mm}^2$
(b)	0.24	$\epsilon_H = 0.06$ (Wall: Al), $\epsilon_L = 0.02$ (Gold-plated radiation shield), $A = 224 \times 170 + 2 \times (224 + 170) \times 10 \text{ mm}^2$
(c)	0.58	$\bar{\kappa} = 0.2 \text{ W m}^{-1} \text{ K}^{-1}$ (Polycarbonate), $A = 16 \times 15 \text{ mm}^2$, $L = 40 \text{ mm}$, 4 posts
(d)	0.20	$\bar{\kappa} = 420 \text{ W m}^{-1} \text{ K}^{-1}$ (Cu), $A = 75 \times 18 \text{ } \mu\text{m}^2$, $L = 100 \text{ mm}$, 300 lines for 10 CCDs
Total	7.22	

Notes.

* See the text.

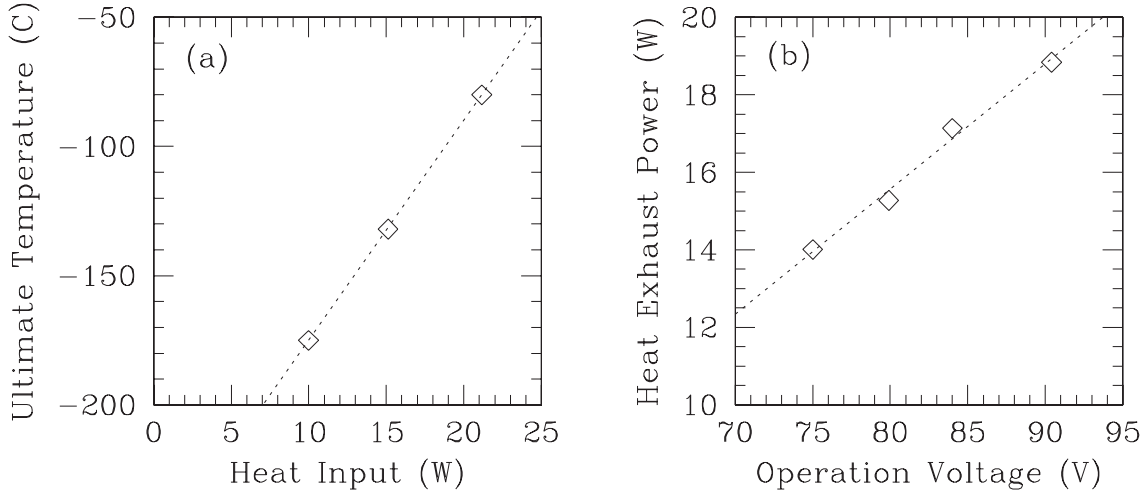


Fig. 10. (a) Ultimate temperature of the cooler head as a function of the heat input to the head. The cooler is operated at the maximum operation voltage (90 V). (b) Heat exhaust power plotted as a function of the operation voltage of the cooler. The cooler head is kept at -100°C .

2.5.3. Cooling system

We adopted a stirling-cycle cooler (Daikin Industries Co., Ltd WE-5000) that runs stand-alone without any external equipment. Daikin claimed that the capacity is 5 W at 80°K ; we tested it by changing the ohmic heat load and verified its capacities. The result is shown in figure 10. The WE-5000 had a capacity of about 16 W at -110°C , where the CCDs are operated. The value was sufficiently larger than the required value of 7.22 W.

The vibration of the cooler could affect the image quality if it induces vibration of the focal plane. In the case that the dewar is heavier than the cooler and is stiffly attached to the mechanical structure of the telescope, it is likely that the induced vibration of the dewar

is small. Inside the dewar the cooler head is connected to a cold plate with a flexible copper braid (38 mm² cross section and 33 mm length) so that the transfer of the vibration becomes small. We measured the degree of vibration of the cold plate using a laser displacement meter (LT8110, Keyence Co., Ltd), and found that the induced vibration is as small as 2 μm (rms) both vertically and horizontally, which is, in fact, negligible compared with the pixel size (15 μm = 0."202).

In order to maintain a sufficiently high vacuum, charcoal is often used as a *getter* of molecules, such as water. This type of getter is, however, practically useless unless it is cooled down to ~ 80 K. Since we use a stirling cooler there is no place where such a low temperature is achieved. We therefore adopted an ion pump (Noble Pump 912-7120; 20 l/s pumping speed; Anelva Co.) as an active getter. The pump has a finite lifetime, which is long enough (20000-35000 hr) if the pump is operated under a high vacuum ($<10^{-5}$ torr).

The cold plate is cooled down to -110°C in 5 hours from room temperature. Once the system is cooled down, the power of the cooler is regulated by monitoring the temperature of the cold plate. Once stabilized, the cooler consumes less than 80% of the maximum operation power i.e., it exhausts about 11 W, which nearly equals the thermal inflow to the dewar. Under this stable operational condition, inside of the dewar is kept below 5×10^{-7} torr at which point the thermal inflow by convection is completely negligible. One drawback of the stirling cooler is that the overhaul maintenance cycle is relatively short, 5000 hours. It is one and a half years if we use the cooler for 10 days per month. The overhaul costs approximately \$15K, which is about one third of the price of the cooler.

2.6. Filters

We have adopted two photometric band systems for broad-band filters, the Johnson-Morgan-Cousins system (Johnson & Morgan 1953; Cousins 1978; Bessell 1990) and the Sloan Digital Sky Survey (SDSS) system (Fukugita et al. 1996). The broadband filters available at the time of this writing were B, V, R_C, I_C of the Johnson-Morgan-Cousins system and g', r', i', z' of the SDSS system. We have built an SDSS u' filter as well, but this filter has not been made available for open use since the transmission of the prime focus corrector is quite low at the wavelengths of this filter. The transmission of the corrector is zero at < 3400 Å and increases to 50% at 3700 Å and 80% at 4000 Å. Note that the QE of the MIT/LL CCDs is also low at UV wavelengths: $\simeq 20\%$ at 3500 Å and $\simeq 50\%$ at 4000 Å.

The specifications for the dimensions of a filter are 205.0 ± 0.5 mm (height), 170.0 ± 0.5 mm (width), and 15.0 ± 0.2 mm (thickness), with a corner cut of C5-C8 (mm) for each of the four corners. The typical weight of a filter is 1.3 kg. A detailed description of the specifications can be found on-line¹.

The filters are made of one or two Schott color-glass elements together with two or

¹ http://subarutelescope.org/Observing/Instruments/SCam/user_filters.html

Table 4. Physical components of the broad-band filters.

Filter	Glass (thickness in mm)	Coating
B	GG385(3) + BG40(3) + BK7*(3) + BK7(6)	short-pass coating
V	GG495(5) + BK7(5) + BK7(5)	short-pass coating
R_C	OG590(5) + BK7(5) + BK7(5)	short-pass coating
I_C	RG9(5) + BK7(5) + BK7(5)	short-pass coating
g'	GG400(3) + BG40(3) + BK7(3) + BK7(6)	short-pass coating
r'	OG550(4) + BK7(3) + BK7(3) + BK7(5)	short-pass coating
i'	RG695(4) + BK7(5) + BK7(6)	short-pass coating
z'	RG695(4) + BK7(5) + BK7(6)	band-pass coating

Notes.

* BK7 is neutral glass.

three neutral-glass elements. A shortpass multilayer interference film is coated on one glass-air surface for $B, V, R_C, I_C, g', r', i'$, and a bandpass multilayer interference film is put between two glass elements for z' . Except for z' , the shape of the transmission at the short-wavelength side is determined by the long-pass transmission of color glass. The physical components of the filters are summarized in table 4.

Laboratory experiments have revealed that the transmission function at the long-wavelength side, which is defined by the coating, of the $B, V, R_C, I_C, g', r', i'$ filters, changes by a nontrivial amount with the temperature and humidity. That is, the cutoff wavelength (wavelength where the transmission is 50% of the maximum) becomes shorter with decreasing temperature and humidity. This is caused by the absorption of water vapor in the air; the maximum amount of the absorption depends solely on the temperature. Since the absorption *saturates* when the humidity exceeds an extremely low threshold, the transmission of filters is expected to shift by the maximum amount for the temperature during the operation of Suprime-Cam ($\approx 0^\circ\text{C}$ with a typical variation of less than 5 deg). It has been found from experiments that the maximum shift of the cutoff wavelength from $T = 20^\circ\text{C}$ to 0°C is $\Delta\lambda = -40$ to -80 Å, depending on the filters. In addition, the cutoff wavelength at the short-wavelength side (except for z'), which is determined by color glass, is also found to depend on the temperature, though the amount of the shift is as small as ~ -10 Å for $\Delta T = -20$ deg. Note, however, that the variation in the temperature at the filter during the operation of Suprime-Cam is typically smaller than ~ 5 deg. Thus, the transmission curve of the filters does not change significantly during the observation. The band-pass film of the z' filter is put between two glass elements, not coated on an air-glass surface, and thus no wavelength shift is seen at either side.

The fast F-ratio, 1.86, also changes the transmission functions of the filters. The change in the part defined by the coating film depends on the filters, and amounts to as large as 50 Å, while the change is negligibly small for the part defined by color glass. Note that the optics of

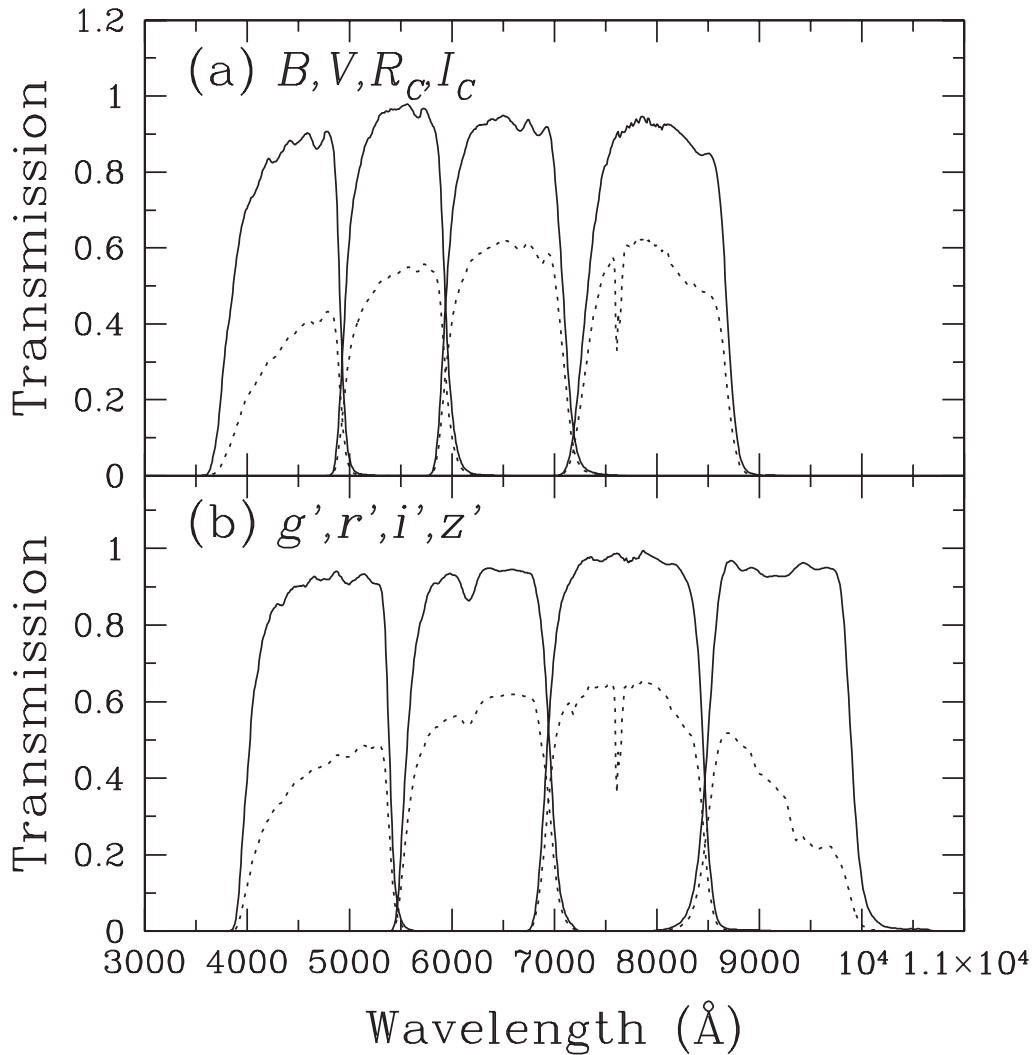


Fig. 11. Transmission curves of Suprime-Cam standard filters (solid line). The dotted lines indicate the combined net responses while considering the CCD quantum efficiency, the throughput of the prime focus corrector, the reflection of the primary mirror, and atmospheric absorption at $\sec z = 1.2$. The deep absorption seen around 7600 \AA is the A-band of molecular oxygen.

the prime focus of Subaru is nearly telecentric. Thus, the angle of light incident on the filter differs at most by only $\simeq 3$ deg over the filter surface. The non-uniformity of the transmission due to this amount of difference is negligible for usual observations.

For each filter, we adopt as the fiducial transmission the one at $T = 0^\circ\text{C}$ for the F/1.86 beam, which is calculated by an extrapolation of the measurement at a room temperature. The fiducial transmission functions of the eight filters are plotted in figure 11 by the solid lines. The dotted lines in the same figure indicate the net responses, which are defined as the combination of the fiducial transmissions with the CCD quantum efficiency, the throughput of the prime focus corrector, the reflection of the primary mirror, and atmospheric absorption at $\sec z = 1.2$. The reflection by the window glass of the dewar is around 1% per surface, since

Table 5. Characteristics of broad-band filters.

Filter	λ_{eff} (Å)	$c(\nu_{\text{eff}})^{-1}$ (Å)	FWHM (Å)	Q
B	4478	4417	807	0.080
V	5493	5447	935	0.092
R_C	6550	6498	1124	0.103
I_C	7996	7936	1335	0.094
g'	4809	4712	1163	0.118
r'	6315	6236	1349	0.127
i'	7709	7633	1489	0.119
z'	9054	9002	955	0.056

an anti-reflection coating is made on both surfaces. Table 5 presents four quantities of these net responses: (i) λ_{eff} , effective wavelength against a spectrum of $f_\lambda = \text{const.}$, (ii) ν_{eff} , effective frequency against a spectrum of $f_\nu = \text{const.}$, (iii) FWHM, and (iv) Q value, which is defined as $\int [R(\nu)/\nu] d\nu$, where R is the net response. Here, λ_{eff} is defined as $\int [\lambda R(\lambda)/\nu] d\lambda / \int [R(\lambda)/\nu] d\lambda$; an extra ν is inserted since the CCD counts the photon number, not the flux, of objects (cf. Fukugita et al. 1995). Similarly, ν_{eff} is defined as $\int [\nu R(\nu)/\nu] d\nu / \int [R(\nu)/\nu] d\nu$.

Suprime-Cam accepts custom-made filters, such as narrow band filters. Any filter for Suprime-Cam should be mounted on a special frame of a filter exchanger, which is described in the next subsection. This imposes rather strict specifications on the filters. Furthermore, after being mounted on the frame, the filter should be tested mechanically in the exchanger in advance of an observation. Those who are interested in making custom-made filters should observe the ‘‘Suprime-Cam filter acceptance policy’’, which can be found at the URL above .

2.7. Filter Exchanger, Shutter and the Control System

2.7.1. Filter exchanger

One of the difficulties in building Suprime-Cam is that the available space at the prime focus is very limited. On the other hand, the size of the filters is significantly large compared to the available space. This fact did not allow us to adopt the conventional filter exchange mechanisms, such as a wheel-type exchanger.

We therefore adopted a different approach to realize the filter exchange. The idea is based on a *jukebox*. A selected filter is first moved horizontally from the stored position to an elevator. The elevator then transports the filter vertically to the focal plane. Finally, the filter is moved horizontally again to be loaded in the operating position. The horizontal transfer is realized by a rack-pinion driving mechanism and the elevator is driven by two ball screws and a stepping motor to achieve precise positioning. A filter holder located between the dewar and the shutter is called the focal box. It has a positioning pin, which secures the position of the filter within the focal box. Each filter has a barcode label and a barcode reader installed on

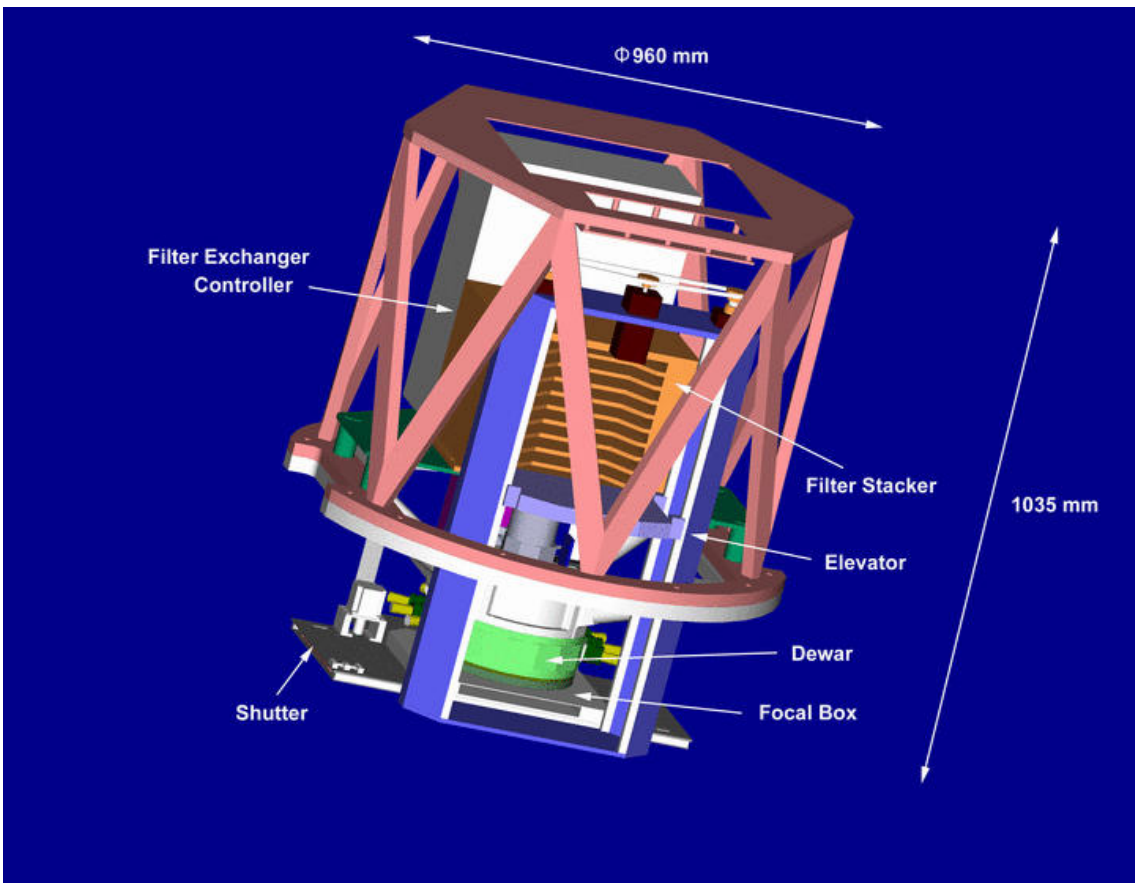


Fig. 12. Schematic view of Suprime-Cam. The major mechanical components are shown inside.

the elevator box double-checks if the right filter is loaded. The jukebox holds up to ten filters at once.

Since each filter including the frame weighs about 3 kg, the horizontal transfer speed of the filter should be limited so that the driving torque becomes sufficiently large. It takes almost 50 seconds for a single horizontal transfer to be completed. A series of filter exchanges (i.e., take a filter out of the focal box, take it back to the slot of the stacker, take the specified filter out of the slot, load it into the focal box) takes about 5 minutes. Note that the elevation of the telescope pointing must be high ($\geq 75^\circ$ is currently required) to reduce the mechanical load on the horizontal transfer system during the filter exchange. This slewing of the telescope introduces another overhead for observing which is typically one minute. Therefore, it takes 6 minutes to complete the exchange. Future upgrade of the filter exchanger is planned to reduce these overhead significantly.

2.7.2. *Shutter*

The physical size of the aperture at the shutter amounts to $205 \text{ mm} \times 170 \text{ mm}$. Since iris-type shutters introduce a significant non-uniformity of the exposure time over such a wide

field of view, we adopted a shutter of the sliding-door type. The space available for the camera in front of the focal plane is only 80 mm (see figure 13). The thickness of the shutter should thus be as thin as possible. We succeeded to develop a large shutter with a thickness of 15 mm.

The shutter has two sliding doors; one door covers the entire aperture. After it slides away to open the aperture, the other door comes in to close the aperture, which guarantees the uniformity of the exposure time. Furthermore, no recovery time is required, since the doors move both ways at the same speed. Two doors are made of *Derlin*, which is a solid, low-friction engineering plastic, and is driven individually with a timing belt and a stepper motor (Oriental Motor UPK543AW). The motor is controlled by pulses generated from the I/O port of Messia-III (see subsection 2.7.3) via a dedicated motor driver. The doors slide on rails made of the Derlin, and their stopping positions are determined by magnetic proximity sensors. It takes 1.03 s to open/close a door and the shortest possible exposure time is set to be 1.2 s. The exposure time is accurate to 0.02 s and uniform to 0.3% over the entire field of view.

2.7.3. *Control system of the mechanism*

Messia-III has two digital signal processors (DSPs): one for CCD control and the other for instrument control. The stepping motors of the shutter are controlled by the pulses from the I/O port of the DSP. The filter exchanger is controlled by a programmable controller (Keyence K2-500) and ladder programs. Messia-III sends commands to/receives status from the controller through the RS-232 communication line.

We installed a small computer system, PCI/104 based CPU (VersaLogic EPM-CPU-6) running Linux associated with the I/O subsystem (VersaLogic VCM-DAS-1), to manage the cooler and the ion pump. Since the cryogenic system are is operated continuously, even during the daytime, we have made its control system completely independent so that the rest system can be shutdown if unnecessary.

System remote reset is realized by cycling AC power to the components. For this purpose, a remote power control module (Black BOX SWI038A) is equipped. The RS-232C port of the module is connected to the control workstation via a RS-232C/optical converter (Black BOX ME570A).

Audio and visual monitoring systems are adopted in the camera frame to diagnose the mechanism of Suprime-Cam. Sounds of the shutter and the filter exchanger are collected by microphones that are attached near them. They also notify observers that an exposure starts/ends or filters are being changed. A small video camera monitors the motion of the filter exchanger. Since the camera is hard to reach once installed on the telescope, these monitors are useful in the case of a possible system failure (e.g., a filter jam) and help to make quick recovery. The video composite signal and audio signals are converted to optical signals by a media converter (Force Incorporated 2792) and sent to a remote observation room.

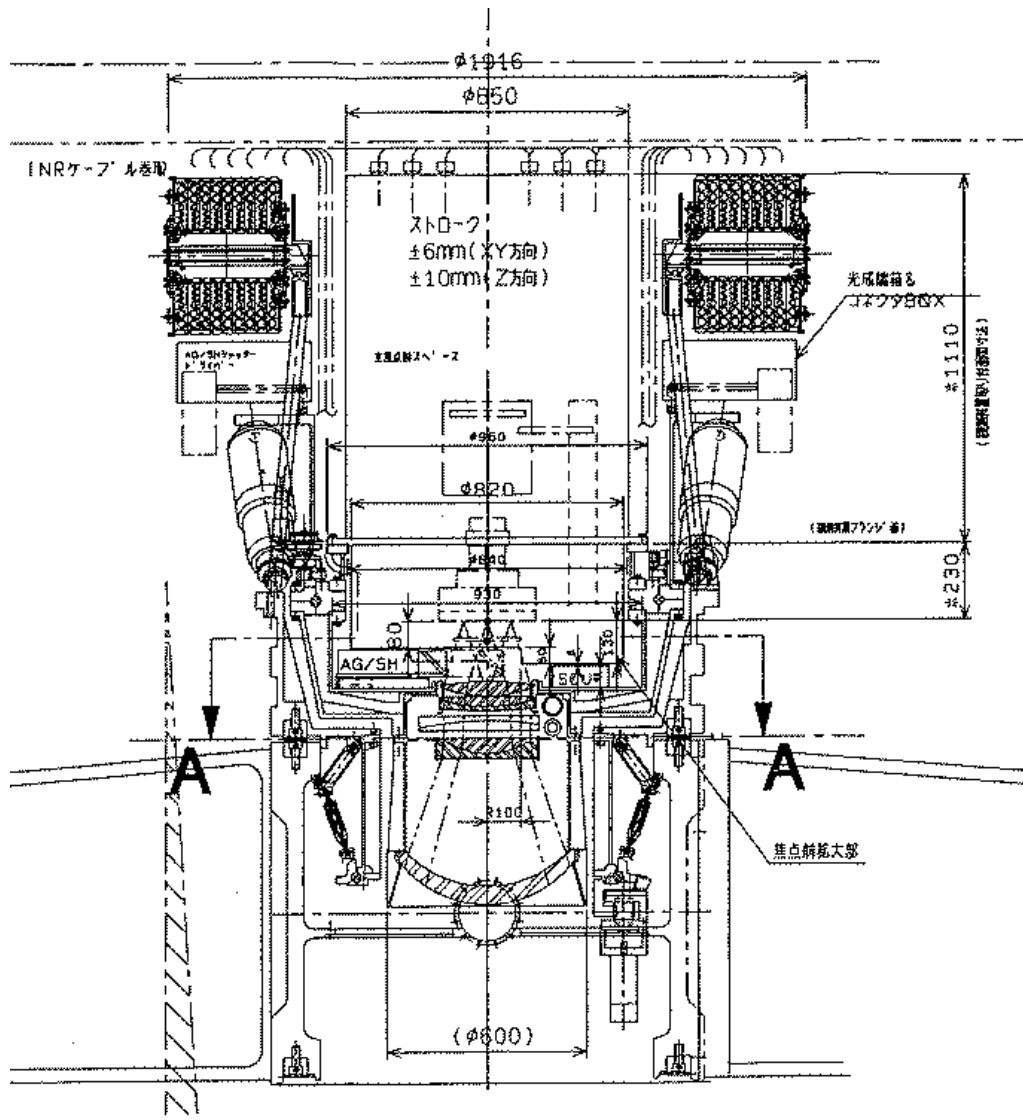


Fig. 13. Cross-sectional view of the Subaru Prime Focus Unit.

2.8. Frame Structure

Figure 13 shows a cross-sectional view of the Subaru prime-focus unit (PFU) where Suprime-Cam is loaded from the top. The PFU is mounted and fixed on the top ring of the telescope. The interface between the telescope and the camera is a torus flange located behind the prime focus by 230 mm. The camera attached to the flange is rotated by the instrument rotator together with an auto guider and a Shack-Haltmann sensor. On the other hand, the wide field corrector is fixed on the PFU. The posture of the PFU is controlled by a so-called Stewart Platform that is supported by six hydraulic jacks.

In order to realize a seeing-limit image over the entire field of view, the focal-plane arrays must be placed within the thin focal depth ($\pm 30 \mu\text{m}$) regardless of the direction of gravity. The

tolerance of the tilt is $30\ \mu\text{m}/100\ \text{mm} \sim 1'$, where 100 mm is the distance from the center to the edge of the arrays. This corresponds to a $120\ \mu\text{m}$ displacement at the interface flange. We therefore set the parallelism between the focal plane arrays and the interface at $100\ \mu\text{m}$. Since reliability is our first priority, we did not employ any active adjustment mechanism. Instead, we machined each component precisely and assembled them step by step by measuring the parallelism accurately at Ishihara Precision.

Figure 12 shows the structure of Suprime-Cam. Four rods extending from the interface secure the vacuum dewar firmly. The rods are made of Invar so as to minimize the thermal deformation. The weight of the dewar, including the cooler and electronics, amounts to 30 kg. FEM calculations showed that the tilt of the dewar is no larger than $0.2'$ regardless of the gravity direction. This was confirmed by actual measurements in the laboratory.

The shutter and the filter exchanger are suspended from the interface flange independently from the dewar. We prepared a stage on the upper part of the flange to fix the filter jukebox, power units and other auxiliary components. The upper part is covered by a truss structure and panels, as shown in figure 12 (panels are not provided to show the inside). All of the feed-through, including optical fibers, power and water coolant, are located on top of the cover. A compact water radiator (LYTRON ES0707) is installed inside the camera and copes with exhaust heat of about 400 W (600 W max) from the components.

2.9. Optics and the Corrector

The design of the prime focus corrector is based on a three-lens corrector for a Ritchey-Chretien hyperboloid mirror (Wynne 1965). Nariai, Yamashita & Nakagiri (1985) determined the positions of the three lenses by balancing the chromatic aberration of the spherical aberration and the image quality at the edge of the field, and also by eliminating any higher order field curvature.

At the late stage of an engineering model study of the Subaru Telescope, it was decided to increase the size of the primary mirror from 7.5 m to 8.2 m. The radius of the curvature of the primary mirror was, however, kept unchanged so that the effects of this change on other design specifications became minimal. Accordingly, the F-ratio of the prime focus changed from 2.0 to 1.83, and the optical design of the prime focus corrector had to be modified. The trade off was between maintaining a 0.5° field of view, while allowing for a slight degradation in image quality and maintaining the image quality by reducing the field of view. The problem was solved by a novel design in which the elements of the atmospheric dispersion corrector (ADC) are also used in optimizing the corrector system (Takeshi 2000; Nariai & Takeshi 1994). Figure 14 shows a schematic view of the optical components of the prime focus corrector, and note that the ADC is fully a part of the corrector.

The ADC consists of one plano-parallel plate and another almost plano-parallel plate. Each of them consists of a plano-convex lens and a plano-concave lens whose radii of curvature

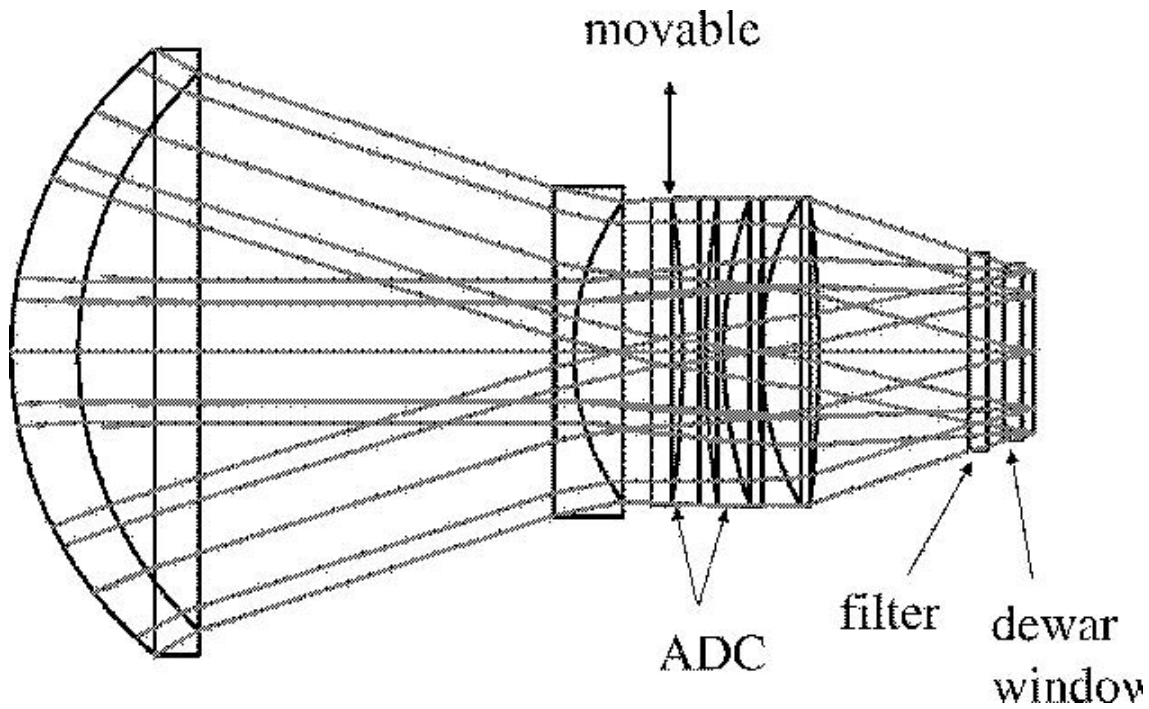


Fig. 14. Prime-focus corrector for Suprime-Cam based on a three-lens corrector design (Wynne 1965), but optimized with additional optical components for ADC.

are the same. The glasses of the two lenses are so chosen that the refractive indices are approximately the same, but the dispersions are different. These two lenses are put together with the curved surfaces facing each other to make a plate. When the plano-parallel plate is shifted perpendicular to the optical axis, it behaves as an ADC. This ADC also acts as an element of the correction of chromatic aberration of the entire system giving one degree of freedom among the secondary spectrum, chromatic differences of aberrations, longitudinal chromatic aberration, lateral chromatic aberration, and the power distribution. Because of this additional one degree of freedom coming from ADC, it was possible to maintain both the image quality and the field of view. This new design also contributed to a reduction of the physical size of the prime-focus corrector.

The fabrication optical data of the prime focus corrector with the melt-data and distances between lenses measured during assembly are given in table 6-4 of Takeshi (2000). They are given here in table 6 for the convenience of readers.

At wavelengths of 0.40-1.0 μm for a zenith distance of 60° or less, the diameter which contains 80% of the energy of a point source at the image plane is less than 22 μm (0."30) for 400 nm, 13 μm (0."18) for 546.1 nm and 23 μm (0."31) for 1000 nm over the entire field of view. More details of including aberration diagrams, spot diagrams, and encircled energy diagrams based on the optical design are given in Takeshi (2000) together with verification measurements during the fabrication of the prime-focus corrector.

Table 6. Fabrication optical data of the primary corrector with the melt-data and distances between lenses measured during assembly.

k	aperture	radius	distance	glass	n_e	$n_{(400nm)}$	$n_{(1000nm)}$	Note
1	8200	*30000	14207.88		1	1	1	
2	506.8	326.76	55.94	BSL7Y	1.518880	1.53097	1.50770	
3	467	319.65	398.5995		1	1	1	
4	275	*-4475.19983	15.856	BSL7Y	1.51854	1.53062	1.50736	
5	251.4	213.36	65.111		1	1	1	
6	(337)	0	25.77	PBM5	1.60743	1.63341	1.58775	
7	(337)	-897.65	13.962	BSM51Y	1.605811	1.62094	1.59239	
8	(337)	0	5.4995		1	1	1	
9	258.6	825.93	14.99	PBM2Y	1.624213	1.65236	1.60319	
10	257.2	391.195	30.451	BSL7Y	1.518550	1.53062	1.50736	
11	257.2	*5355.97529	0.836		1	1	1	
12	257.3	268.24	48.083	S-FPL51	1.498524	1.50774	1.49027	
13	254.5	-1098.3	125.50955		1	1	1	
14			15.0	SiO ₂	1.460280	1.47032	1.45056	filter
15			14.5		1	1	1	
16			15.0	SiO ₂	1.460280	1.47032	1.45056	window
17			10.0		1	1	1	
18								image

k	r	e ²	B	C	D	D'	E
1	30000	1.00835					
4	-4475.19983		3.38267E-9	-8.36303E-14	2.03782E-18	-1.33838E-20	3.49307E-23
11	5355.97529		1.30769E-9	-5.38888E-14	-6.67037E-18	6.94170E-20	-2.28747E-22

Notes.

* Aspheric constants

$$x = (h^2/r)/(1 + \sqrt{1 - (1 - e^2)(h/r)^2}) + Bh^4 + Ch^6 + Dh^8 + D'h^9 + Eh^{10}, \quad h = \sqrt{y^2 + z^2}.$$

Suprime-Cam is controlled by a main program running on a SPARC workstation with dual 168 MHz Ultra-2 CPUs, 1.4 GB memory, and a 47 GB Ultra-SCSI RAID-5 local disk. The main program communicates with several other programs running in parallel: DSP programs running on Messia-III that control the CCD and the shutter, ladder code programs running on the controller of the filter exchanger, and a status monitor (figure 1).

The CCD readout is performed by a DSP program in the CCD controller (figure 15). In response to a command from the main program, the DSP program generates a CCD clock waveform, and a stream of unsigned short data from the AD converter is stored into the local memory on Messia-III. Once the clocking comes to an end, a command of data transfer from the local memory to the shared memory of the main WS is initiated by the main program. After being transferred to the shared memory, the data are de-scrambled into 10 simple 2-dimensional 16-bit FITS data so that each file corresponding to a CCD chip keeps the same orientation as in the observation. Meanwhile, the FITS header is prepared by the main program. The header and the data are then merged, written to the hard disk, and sent to an archiver. While it takes 50 seconds to read out all CCDs, there is additional overhead between exposures, including wiping CCDs (8 s), transferring data from Messia-III to WS (52 s) and handling the data on the WS (10 s), which is 2 minutes in total².

The shutter is controlled by a DSP program, which uses interrupt signals from the Real Time Clock (RTC) on board Messia-III to ensure the preciseness of the exposure time regardless of the load of main WS. The precision is less than 1 ms. For the filter exchanger, the main program sends command strings, such as “initialize”, “set filter”, or “restore filter” to Messia-III. It simply passes the strings to the filter exchanger controller via RS-232C. When “set filter” command is issued, the controller also reads the barcode of the filter which is going to be loaded into the focal box to check if it is the correct filter, and returns the status to the main WS.

The status monitor of Suprime-Cam is implemented as a CGI (Common Gateway Interface) program. CGI is a standard WWW technique for sending dynamic information. The current status of the components and internal status of the main program are written into the shared memory of the main WS and constantly updated. The CGI program reads the memory and formats the current status into HTML (figure 16). As the monitor program is a CGI, any WWW browsers can be used as a remote status monitor. We did not develop our GUI clients, because the evolution of GUI is currently very rapid. Using HTTP, CGI, and HTML, which are stable and standard protocols for sending formatted information, we can easily maintain the status monitor.

² In 2002 August right after submission of this paper, we upgraded the electronics Messia-III to the new one Messia-V (Nakaya 2002 in prep.) as well as the local WS to an 2.2 GHz dual Pentium-based Linux box. The overhead is now shortened down to 58 s. Recent statistics shows that the ratio of total exposure time to usable observing time during the night reaches up to 80% on average.

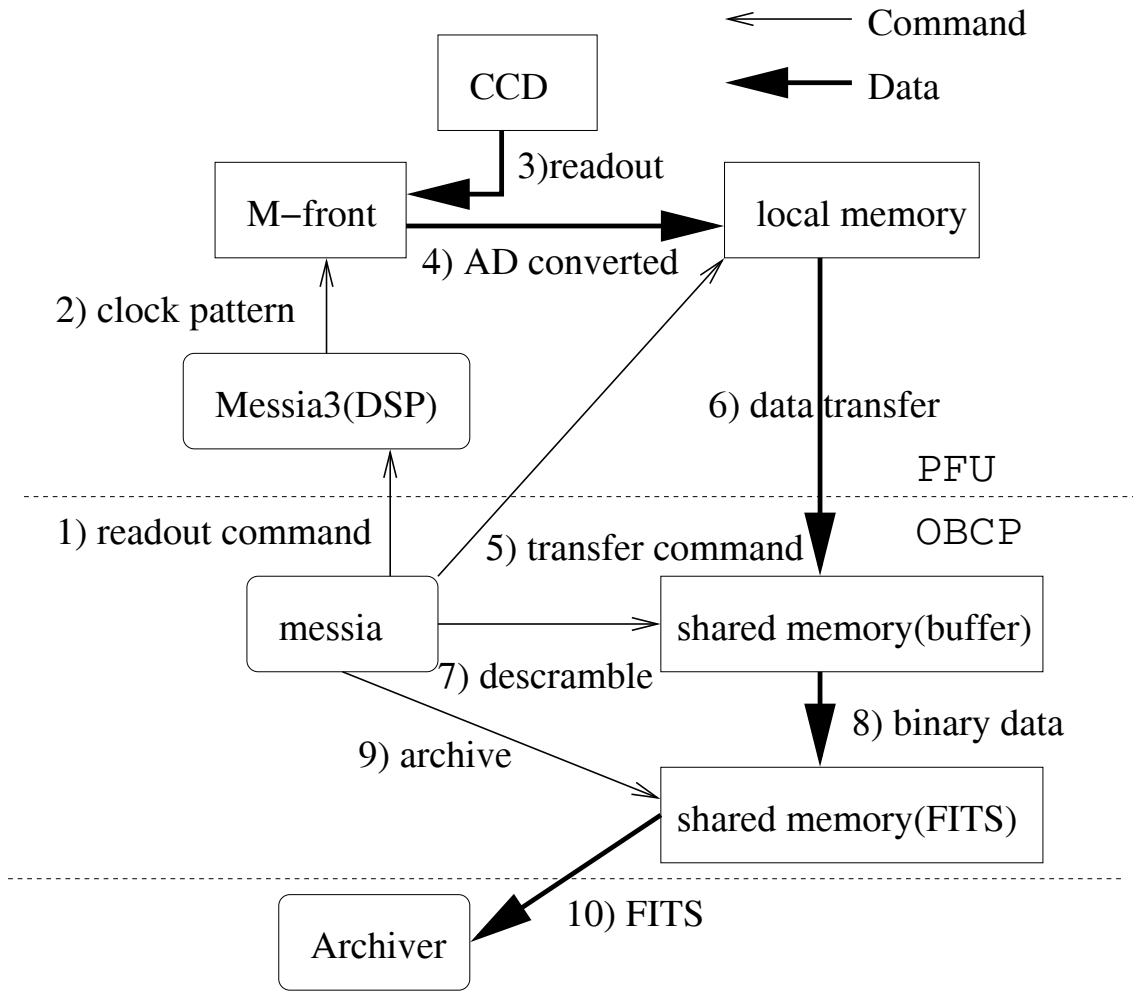


Fig. 15. Command and data-flow diagram of reading the CCD. Command flow is expressed as the thin arrows, and data flow as the thick arrows.

During an observation, Suprime-Cam is controlled from the Subaru Observation Software System; SOSS (Kosugi et al. 1997; Sasaki et al. 1998). The telescope control, data archive, and main program of Suprime-Cam are commanded from a scheduler process in the master control WS in SOSS, and act as slave processes. Since the control is centralized in the scheduler process, the observation with Suprime-Cam is highly automated. Such an automation is implemented aiming for future queue observations and service observations. The scheduler also controls the synchronicity of commands so that the dead time should be minimum.

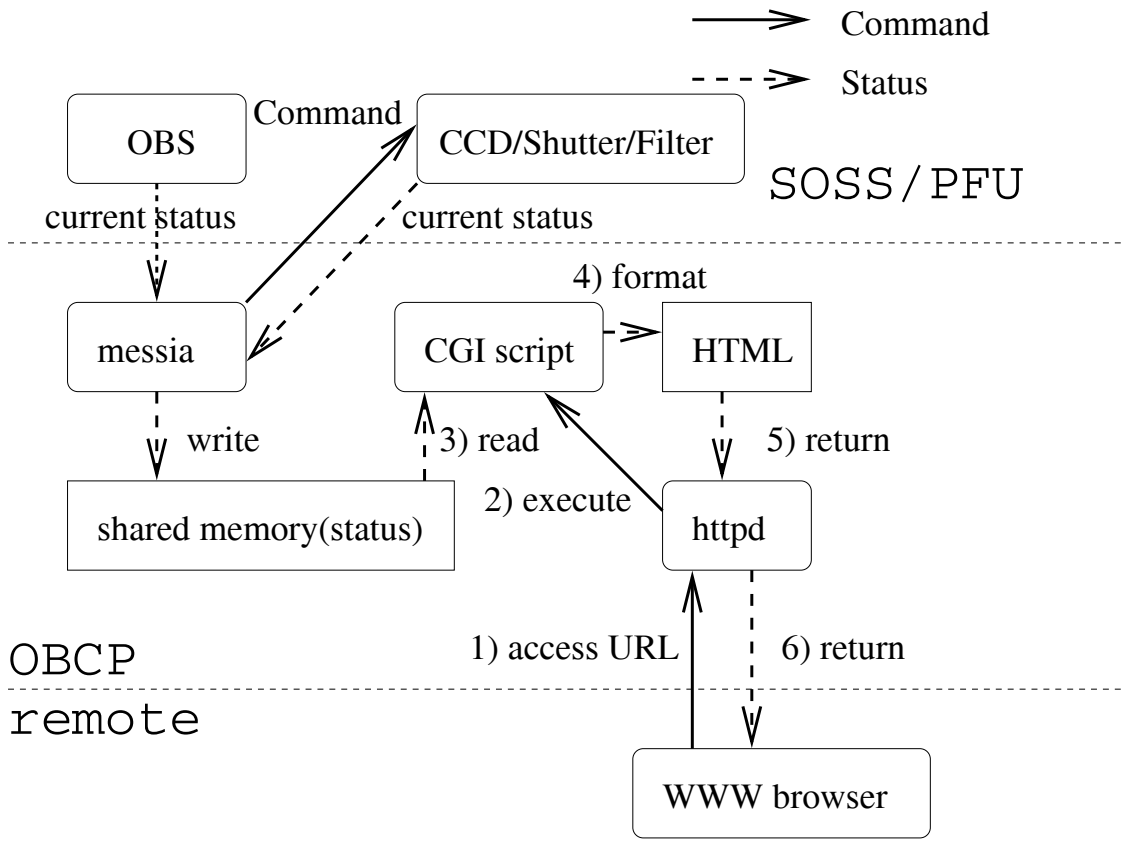


Fig. 16. Command and data flow diagram of the status monitor. Command flow is expressed as the solid arrows, and status as the dashed arrows. The status from the master control WS, the CCD electronics, the shutter controller and the filter-exchanger are written into the shared memory and always updated by the main program. Users access to httpd running at the instrument control WS and receive the current status in HTML format.

3. Performance Verification

3.1. Optical Performance

3.1.1. Alignment of the wide field corrector

There are three main factors that affect the image quality of the camera: the primary mirror, the wide-field corrector and telescope tracking. Image degradation due to the primary mirror is controlled to be well below $0.''2$ FWHM, judging from results of Shack-Hartman tests. Image degradation due to the wide-field corrector is smaller than $0.''27$ FWHM, as described in subsection 2.9. The telescope tracking error has been proved to be less than $0.''07$ for a typical ten-min exposure when assisted by an auto guider under negligible wind condition that might cause the shaking of the telescope. Since the quadratic sum of the three components is $0.''34$, the normal seeing (typically $\geq 0.''4$) dominates the image-quality degradation once all the adjustments of optics are made appropriately.

We introduce the ellipticity of a stellar image, which is a measure of the PSF anisotropy,

which is useful to diagnose any adjustments of the optics, defined by

$$\{e_1, e_2\} = \{I_{11} - I_{22}, 2I_{12}\} / (I_{11} + I_{22}). \quad (5)$$

The moments, I_{ij} , are calculated by

$$I_{ij} = \int d^2x W(\vec{x}) x_i x_j f(\vec{x}), \quad (6)$$

where $f(\vec{x})$ is the surface-brightness distribution of a stellar image and $W(\vec{x})$ is a Gaussian weighting function (Kaiser et al. 1995).

The first step of the adjustment is alignment of the optical axis of the wide-field corrector to that of the primary mirror. If the misalignment is small, its two components, the decentering and the tilt, can be treated separately. The decentering causes coma aberration while the tilt causes astigmatism. Since the coma aberration is almost uniform over the field of view, it is sufficient to measure it at some small portion of the field. In fact, the decentering was measured and corrected through a Shack-Hartmann test performed near the field center, which controls not only the decentering of the corrector, but also the shape of the primary mirror.

The shear induced by the astigmatism, on the other hand, is a function of the field position. It is efficient to use Suprime-Cam, which covers most of the field at once, to measure the shear. For example, if the tilt amounts to θ_y around the Y-axis, we note that the ellipticities of stars, \vec{e} defined by equation (5), can be well approximated as

$$\vec{e} = k\theta_y \vec{x}, \quad (7)$$

where \vec{x} is the field position relative to the optical axis and k is a constant which is dependent on the degree of defocus. An example of the ellipticity map is shown in figure 17, where the mean ellipticities of stars in 11×11 partitions in the field of view are shown illustrated by ellipses. By measuring the ellipticities of stars over the entire field we can estimate the direction and degree of the tilt at the same time based on equation (7). After repeating the cycle of measurement and the adjustment several times, we were able to make the tilt below 0."5, which was sufficiently small. We monitored the tilt by changing the elevation of the telescope and no apparent change of the tilt was seen.

3.1.2. Coplanarity of the focal plane

We examined the coplanarity of the focal plane composed by 10 CCDs. An exposure of 10 seconds was made through the I_c band filter under a seeing of $\sim 0."$ 4 by changing the focus position. Figure 18 shows the stellar image sizes averaged over each of ten CCDs plotted as a function of the focus position. Since the best focus position is the same for all of the CCDs, as can be seen in figure 18, the co-planarity of the focal plane seems to be accomplished at a satisfactory level, i.e., any deviation from coplanarity is not visible even under superb seeing. The figure also shows that an image quality as good as 0."4 can be achieved on Suprime-Cam, which proves that the three components mentioned in subsection 3.1.1 remains minimal, indeed.

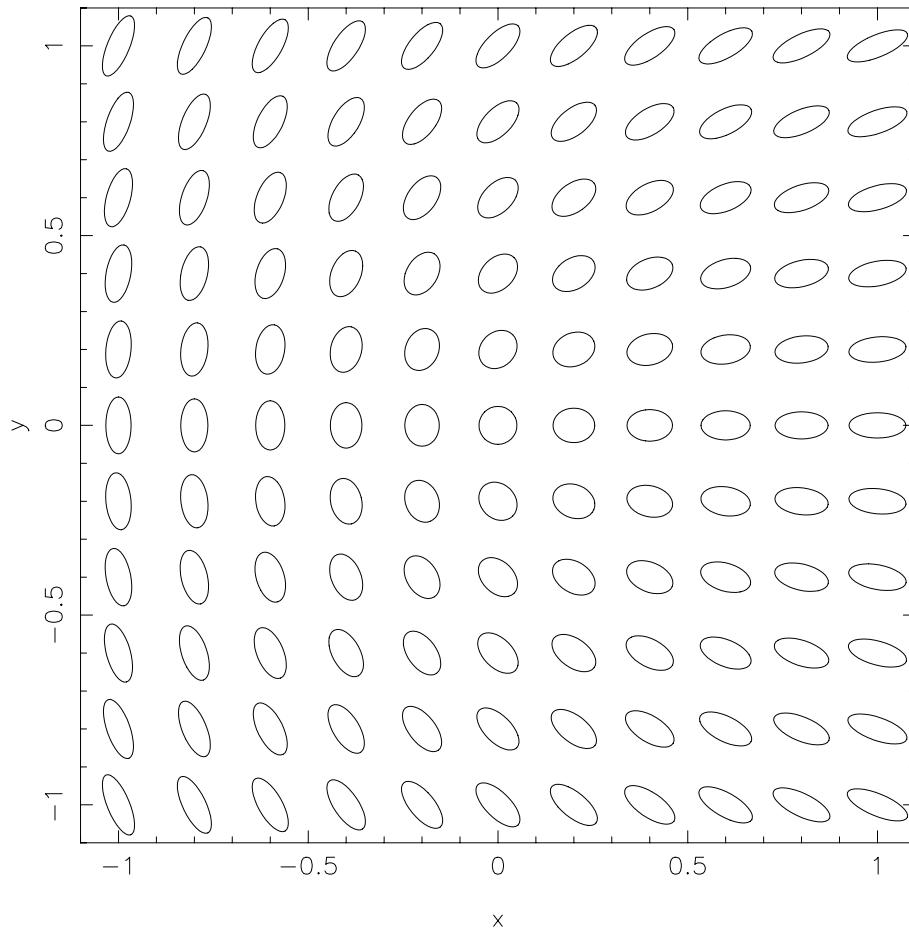


Fig. 17. Example of an ellipticities map ($\vec{e} = 0.5\vec{x}$; see the text) showing the astigmatism induced by the tilt along the Y-axis of the optical axis of the wide-field corrector with respect to that of the telescope. The mean ellipticities of stars in 11×11 partitions in the field of view are illustrated by the ellipses.

3.1.3. Seeing statistics

We monitored the seeing during the commissioning phase over a period of one and a half years. The data are based on images taken for the focus adjustment procedure; the results are shown in figure 19. The closed circles show the data taken in the I_c band, including a similar i' band, which are the most frequently used bands, and the open squares show the data of all other bands. The median seeing is $0.''61$ in the $I_c(i')$ band and $0.''69$ when all of the bands are taken into account. The best seeing that we have ever obtained was $0.''37$ in an I_c band image of 180 s exposure. The image of $0.''4$ - $0.''45$ seeing is routinely obtained at longer wavelength (redder than V -band) with an exposure time of typically 5 to 10 min.

3.1.4. Image quality of Suprime-Cam

The left panel of figure 20 shows the stellar ellipticities measured on a certain image of 6 min exposure in the R_c band. The seeing size of the image is $0.''6$, a typical value. The mean value of the ellipticities over the field of view is about 2% and the standard deviation, σ_e , is

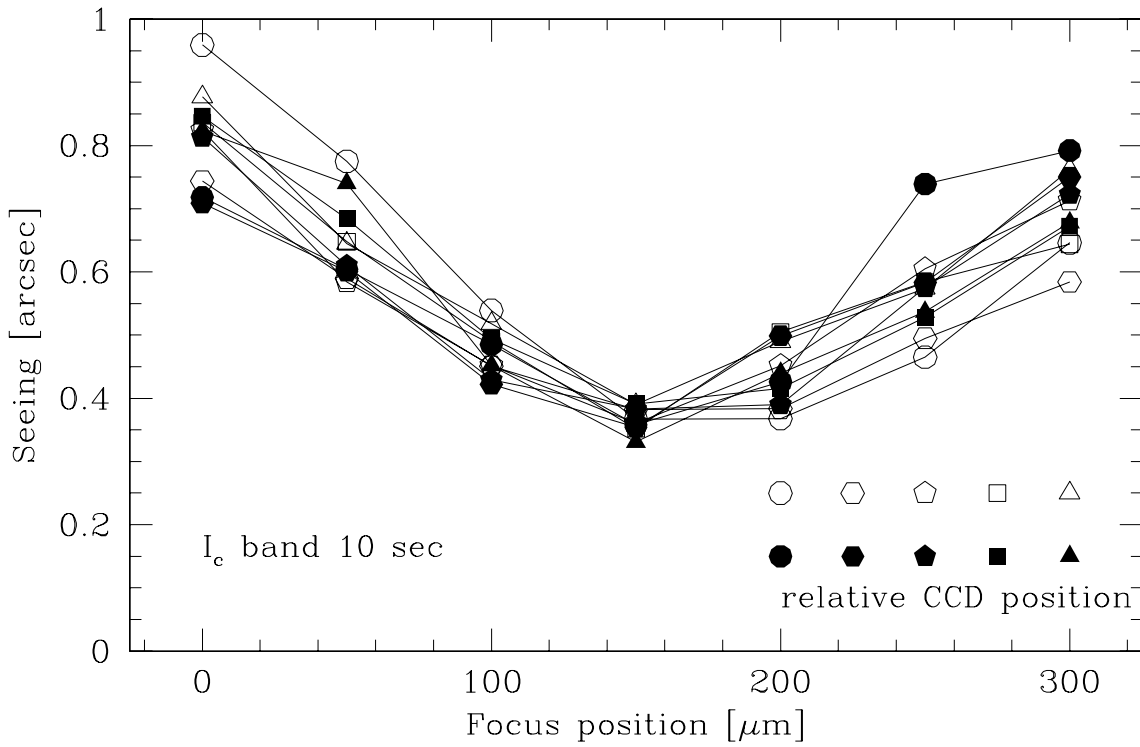


Fig. 18. Stellar image sizes averaged over each of the ten CCDs as a function of the focus position. The exposure is in the I_c band and the integration time is 10 s at each position.

about 1.5%. These values are quite small compared with those of a camera mounted on an earlier generation telescope. For example, UH8K mounted on CFHT shows 5-7% ellipticities according to van Waerbke et al. (2000). This demonstrates that we achieved sufficiently good optical and mechanical adjustments of the telescope/camera system.

3.1.5. Deriving the distortion parameters

A science exposure usually consists of several stacked images. Image stacking is not a trivial procedure because of the large distortion of the optics. Here, we describe how to derive the distortion parameters. We employ a geometrical model of field distortion using a 4th-order polynomial function,

$$\frac{R - r}{r} = ar + br^2 + cr^3 + dr^4, \quad (8)$$

where R and r are the distances from the optical axis in units of pixel on the CCD coordinates and the celestial coordinates, respectively. The displacement and the rotation of each CCD from its nominal position, $(\Delta x, \Delta y, \Delta \phi)_c$, are set as free parameters. We change the telescope pointing typically by 1'-2' between successive exposures. The offset and the rotation of the telescope pointing between the exposures, $(\Delta X, \Delta Y, \Delta \Phi)_e$, are set as free parameters as well. All of these parameters can be determined by minimizing the distance of the same stars identified on different exposures. The residual of the distances is a measure of the error of this mosaic-

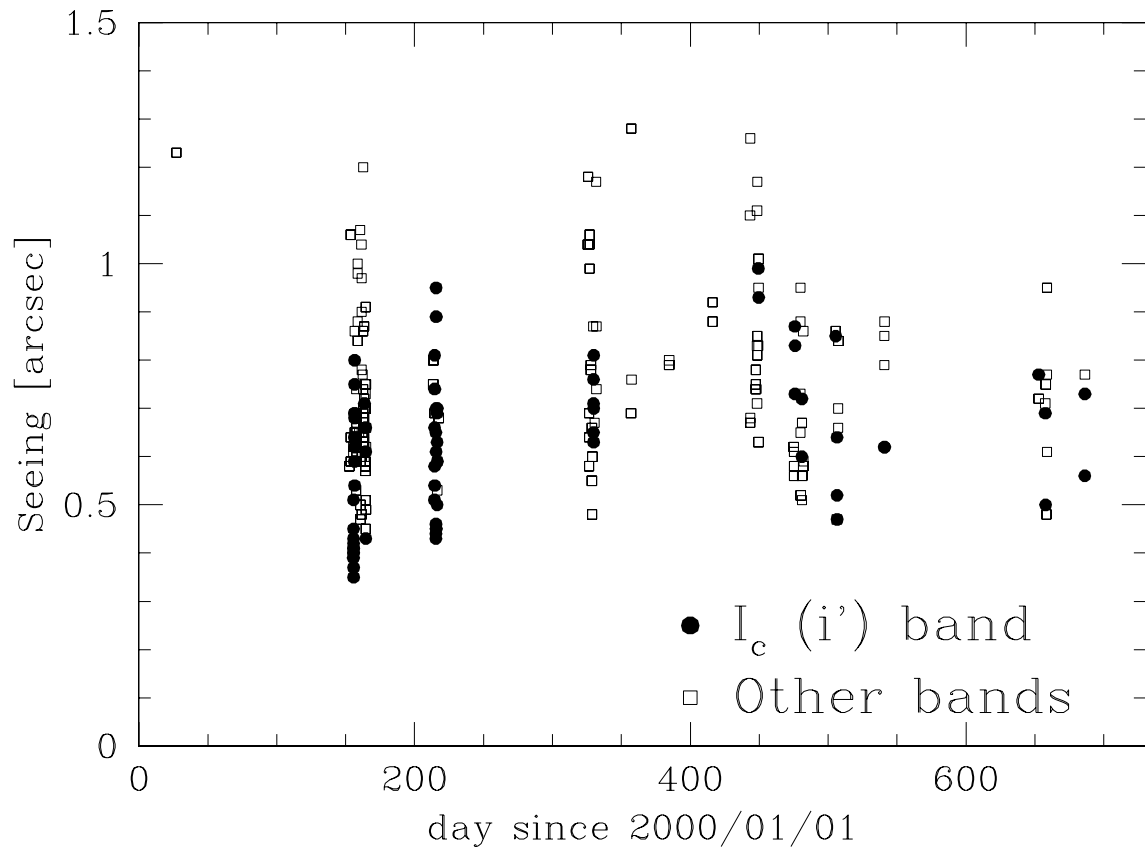


Fig. 19. Long-term seeing statistics of Suprime-Cam. The closed circles represent the data taken in the I_c or i' band, which are the most frequently used filters, and the open squares show the data for all other bands. The median seeing is $0''.61$ in the $I_c(i')$ band and $0''.69$ when all bands are taken into account.

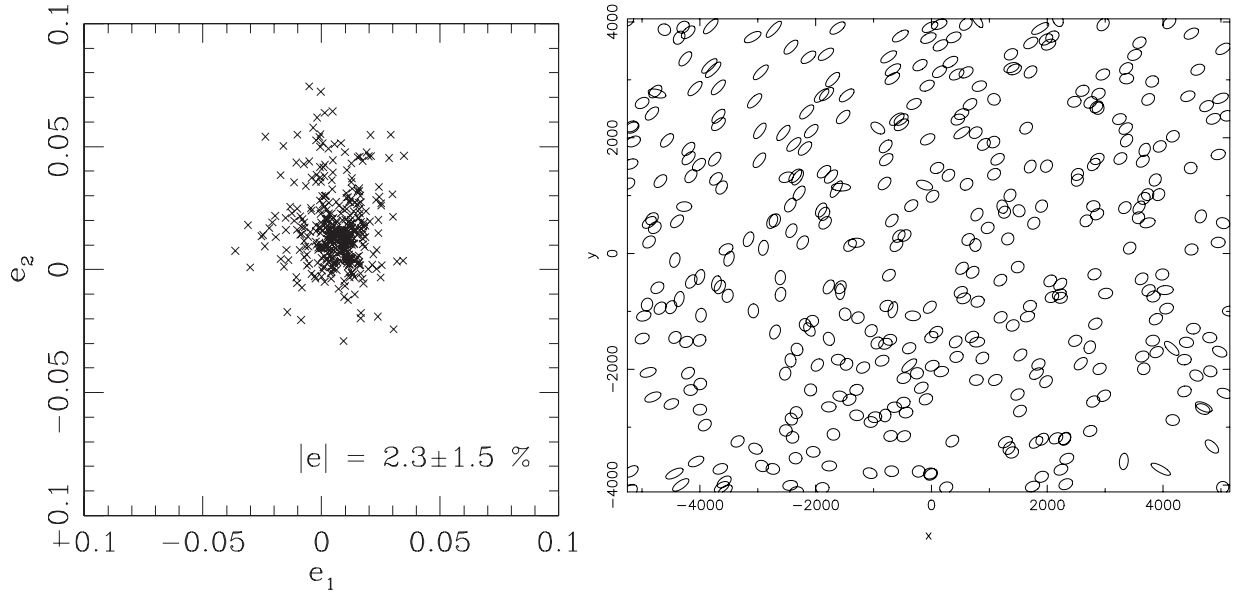


Fig. 20. Ellipticities of stars evaluated on a certain single image of $0''.6$ seeing (left) and the ellipticity map (right) where the ellipticities are ten-times exaggerated for clarity.

Table 7. Parameters of the optical distortion.

a	b	c	d
7.16417×10^{-8}	3.03146×10^{-10}	5.69338×10^{-14}	-6.61572×10^{-18}

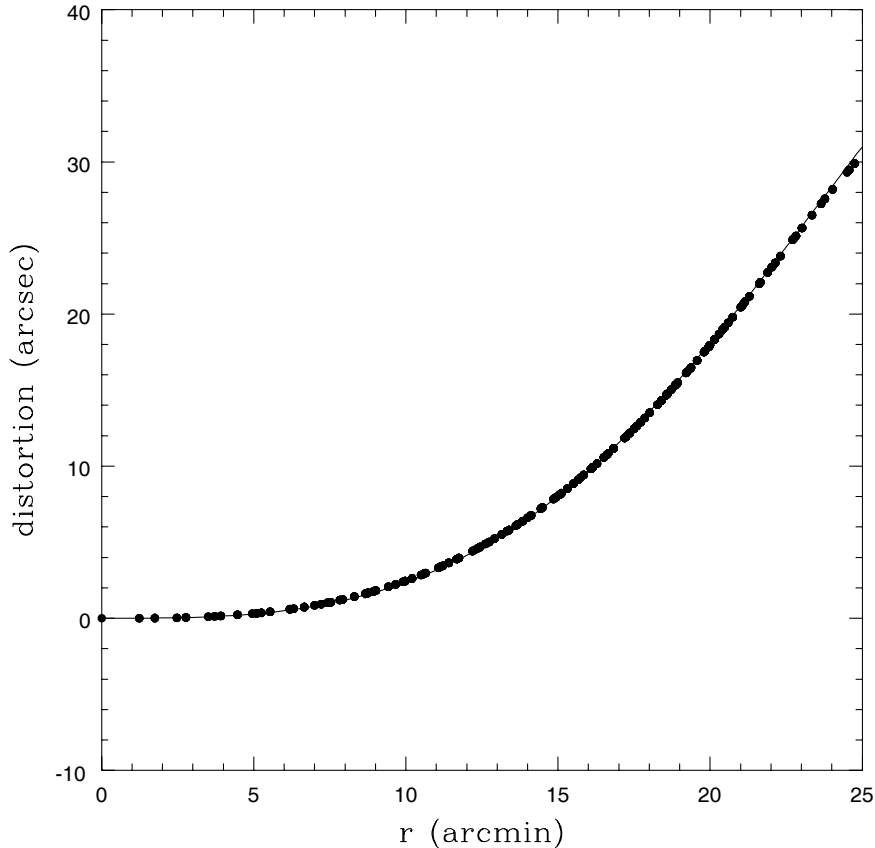


Fig. 21. Optical distortion of the prime-focus corrector. The solid circles represent the distortion calculated by ray-tracing and the solid line shows the geometrical solution of Suprime-Cam (see text). Both agree quite well, which implies the reliability of the solution.

stacking procedure. The rms value of the residuals is typically about 0.5 pixel.

The distortion parameters determined by this procedure are summarized in table 7. Figure 21 shows the distortion computed based on our model with the parameters given in table 7 compared with that calculated by a ray-tracing program. The measured distortion agrees quite well with the computation, which suggests that the solution of the geometry is reliable. The displacement (t) and the rotation (ϕ) of each CCD are consistent with the allowance of fitting ($\Delta r = 30 \mu\text{m}$) between the alignment pins and the holes of the CCD mounting (subsection 2.3.2), and are found to be stable ($dt \sim 4 \mu\text{m}$, $d\theta \sim 0.05$ rad for about a year), which is natural.

3.2. Limiting Magnitude

3.2.1. Magnitude zero points

We derived the magnitude zero point, i.e., the AB magnitude corresponding to a flux of 1 ADU per second, for the B, V, R_C, i' , and z' bands using data of photometric (B, V, R_C) and spectrophotometric (i', z') standard stars taken in the commissioning phase of Suprime-Cam. Table 8 presents the results at an airmass of $\sec z = 1.2$, together with predictions for $\sec z = 1.2$ calculated with the system throughput we evaluated, which are also given in the table. The typical uncertainties in the observed and predicted values were estimated to be $\sim \pm 0.05$ and ± 0.1 magnitude, respectively. It is found that the predictions agree with the observed values with discrepancies of less than ± 0.07 mag. This demonstrates that we have correctly evaluated all of the factors, including the telescope optics, that contribute to the total throughput of Suprime-Cam.

3.2.2. Limiting magnitudes

We estimated the limiting magnitudes for a 1-h exposure for the B, V, R_C, i' , and z' bands based on deep imaging data taken during the commissioning phase. We used data of the Subaru Deep Field [SDF; a blank field centered at $RA(2000) = 13^h 24^m 21.^s 4$, $DEC(2000) = +27^\circ 29' 23''$] for B, V, i', z' , and those of CL1604 + 43 a distant cluster at $z \simeq 0.9$) for R_C . The SDF is one of the two deep fields observed with Suprime-Cam to study the properties of distant field galaxies. These data were taken on dark, mostly clear nights. Their image quality was on the average good, with a seeing size of $0.''6$ - $0.''8$.

The estimated limiting magnitudes in the AB system are summarized in table 9. Here, the limiting magnitude is defined as the brightness corresponding to $3\sigma_{\text{sky}}$ on a $2''$ -diameter aperture, where σ_{sky} is the sky noise measured as the standard deviation. Column 2 of table 9 shows the limiting magnitude for a 1-h exposure scaled from the raw value for the exposure time shown in the parentheses (column 3) made at the field given in column 4.

For the reader's reference, we plot in figure 22 the galaxy number counts for B, V, R_C, i', z' derived from the SDF data. The net exposure time of R_C for the SDF was 73 min. The solid circles indicate the counts in the SDF, where incompleteness of detection at faint magnitudes has not been corrected. The counts at brighter than ~ 18 - 20 mag are not plotted because images of such bright galaxies often suffer from saturation and, thus, were removed in our analysis. At the faintest magnitudes, the observed counts reach $\simeq 2 \times 10^5$ (B, V, R_C, i') and 1×10^5 (z') gals $\text{mag}^{-1} \text{deg}^{-2}$. The turnovers seen at the faintest magnitudes are artifacts due to the incompleteness of detection. The open circles in panels (a), (b), and (d) show the counts for $B450$ (a), $V606$ (b), and $I814$ (d) in the Hubble Deep Field North (HDFN, Williams et al. 1996). The counts in the SDF agree reasonably well with those in the HDFN. Note that the actual number of galaxies exceeds 100000 per field of view ($R_c < 27$, 73 min exposure), which demonstrates that Suprime-Cam substantially improves the efficiency of statistical studies of

Table 8. System throughput and magnitude zero points.

Band	B	V	R_C	i'	z'
Zero point (AB mag)*					
Measured	27.40	27.54	27.70	27.92	27.05
Calculated	27.42	27.58	27.70	27.85	27.03
Throughput					
Mirror	0.91	0.90	0.89	0.86	0.90
Corrector	0.85	0.92	0.93	0.92	0.85
CCD	0.61	0.75	0.84	0.85	0.54
Filter	0.88	0.97	0.94	0.96	0.93

Notes.

* Typical airmass (sec z) of 1.2 is assumed.**Table 9.** Limiting magnitudes of Suprime-Cam*.

Band	AB mag (1hr)	AB mag (exp.time)	Field
B	27.2	27.7 (151 min)	SDF
V	27.1	27.4 (109 min)	SDF
R_C	26.8	26.4 (30 min)	CL1604
i'	26.5	26.8 (103 min)	SDF
z'	25.9	26.0 (68 min)	SDF

Notes.

* These data were taken on dark, mostly clear nights. Their image quality was on the average good, with a seeing size of 0."6-0."8.

faint galaxies.

3.3. Comparison with Other Systems

The observing time of large-aperture telescopes ($D > 4$ m) was once thought to be devoted primarily to spectroscopic observations, since imaging can be made with smaller telescopes. Wide-field imaging with large telescopes, however, has gradually drawn astronomers' attention since several pioneering discoveries were reported, including weak lensing induced by dark matter (Tyson et al. 1990), Lyman break galaxies (Steidel et al. 1996), Lyman alpha emitters (Cowie & Hu 1998) and high redshift type Ia supernovae (Perlmutter et al. 1997). The advent of large format CCDs ($\sim 4k \times 2k$ pixels) around 1994 made the efficiency of imaging observations quite high, and interests in imaging with large telescopes became much stronger.

Table 10 presents comparisons of Suprime-Cam with other wide-field mosaic cameras. In the table, A shows the light-collecting power of the telescope measured by the area of the primary mirror, and Ω is the field of view in square degree. Thus, $A\Omega$ represents a measure of

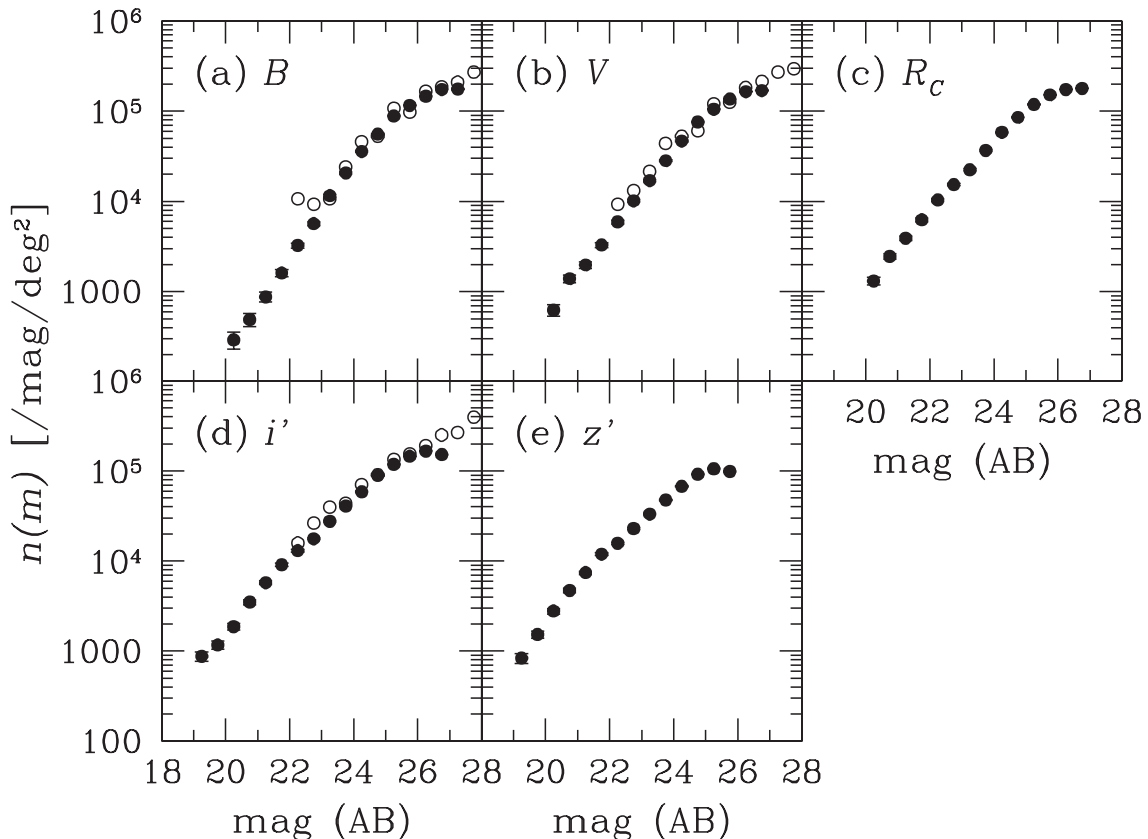


Fig. 22. Differential galaxy number counts for B, V, R_C, i', z' in the data of the Subaru Deep Field (solid circles). Any incompleteness of detection at faint magnitudes has not been corrected. Counts at brighter than ~ 18 - 20 mag are not plotted, because such bright galaxies are often saturated, and were, thus, removed in our analysis. The open circles in panels (a), (b), and (d) show the counts for $B450$ (a), $V606$ (b), and $I814$ (d) in the Hubble Deep Field North (Williams et al. 1996).

the survey speed of the camera, although the exact survey performance depends on numerous factors, including the camera duty cycle, available number of nights for the survey and so on, which we do not deal with here. The SDSS photometric camera is certainly the most powerful instrument in terms of $A\Omega$ although deep survey is not appropriate for the camera because of the moderate seeing ($\sim 1.''2$) of the site. In fact, the SDSS camera has a relatively coarse resolution of $0.''4$ /pixel optimized for the wide survey to which it is dedicated. The largest aperture of Subaru gives Suprime-Cam the highest $A\Omega$ among the cameras built so far for the large telescopes that pursue objects as faint as possible. The exposure time one needs to reach up to a given magnitude is shorter for larger apertures. Thus, Suprime-Cam is the most powerful camera for detecting faint transient objects. The excellent image quality demonstrated in subsection 3.1 is also a distinctive feature of Suprime-Cam.

Cameras with a much wider field of view are being built or planned, as listed in table 10. These are motivated by a widely accepted consensus that the progress of observational astronomy is simply limited by the available telescope time. *MegaCam* (Boulade et al. 2000), which

Table 10. List of selected mosaic CCD cameras.

Camera Name	Telescope				CCD			FOV	$A\Omega$	First Light
	Name	D [m]	A [m ²]	F	Vendor	Format	N_{CCD}	Ω [deg ²]		
WFPC2	HST	2.5	3.46	12.9	Loral	800×800(15)	3	0.0015	0.005	Dec-93
ACS	HST	2.5	3.46	12.9	SITe	4k2k(15)	2	0.0031	0.011	Apr-02
UH8K	CFHT	3.6	9.59	4.2	Loral	4k2k(15)	8	0.25	2.40	Sep-95
SDSS	SDSS	2.5	3.83	5	SITe	2k2k(24)	30	6.0	22.99	May-98
NOAO8K	Mayall	3.8	9.98	2.7	SITe	4k2k(15)	8	0.36	3.59	Jul-98*
CFH12K	CFHT	3.6	9.59	4.2	MIT/LL	4k2k(15)	12	0.375	3.60	Jan-99
Suprime-Cam	Subaru	8.2	51.65	2.0	MIT/LL	4k2k(15)	10	0.256	13.17	Jul-99
MegaCam	CFHT	3.6	9.59	4.2	Marconi	4.5k2k(13.5)	40	1	9.59	2002
Pan-STARRS	Pan-STARRS	2.0	2.14	4.0	MIT/LL	4k4k(12)	64×4 [†]	7×4 [†]	15×4 [†]	2006
LSST [‡]	LSST	8.4	37.40	1.25	(TBD)	(1k1k(10))	(1300)	(7.1)	265.54	2009

Notes.

* after the CCD upgrade to SITe'

[†] Pan-STARRS is an array of telescopes. Initially, four telescopes will be built.[‡] formerly called Dark Matter Telescope; based on a report of a workshop, Science with the Large-aperture Synoptic Survey Telescope, Tucson, Arizona, Nov 17-18, 2000.

is being built for the 3.6 m CFHT, and is scheduled for the first light in 2002, has an $A\Omega$ value comparable to that of Suprime-Cam because of the wider field (1 deg²). Kaiser et al. (2002) worked out a new scheme for a small telescope array in cooperation with innovative orthogonal transfer CCDs (Tonry et al. 2002) to realize high-resolution wide-field imaging. The project is funded and four telescopes will be built by 2006. Tyson & Angel (2001) are proposing Large-aperture Synoptic Survey Telescope (LSST), which is an 8.4 m telescope with about 7 deg² FOV dedicated for only wide field imaging surveys. To remain competitive in this new era of wide-field imaging, an upgrade of Suprime-Cam is crucial in the very near future. For example, a widening of the field of view up to 4 deg² would make $A\Omega$ about 207, which is comparable to that of LSST. This is no doubt challenging and requires a complete re-design of the prime focus unit and the corrector. Recent optical design shows that the new corrector with the first lens of 1.5 m in diameter (d) can realize an image quality better than 0."3 (diameter of 80% encircled energy) over the field of view if we allow field curvature of the focal plane and only consider $\lambda \geq 550$ nm. We are currently trying to reduce the size of the first lens down to $d \sim 1.2$ m ϕ , which we hope to fabricate using fused silica, without any significant loss of the image quality.

4. Conclusion

We have designed and built a wide-field camera for the prime focus of the 8.2-m Subaru telescope, which we named Suprime-Cam. Table 11 shows the main characteristics of the cam-

era. Suprime-Cam is currently provided for open-use observations by Subaru and has become one of the most frequently used instruments among others. Nearly 30% of all nights is allocated to the camera as of this writing. This, we think, is because Suprime-Cam has an outstanding survey speed under sub-arcsec seeing, which is unique within the suite of instruments available on very large telescopes. There has been no serious trouble which has stopped observing, although the burden of operations has not yet been quite minimized. For example, new filters require extensive trial-run for mechanical shakedowns. We will redesign some mechanics so as to reduce such operational costs. In the meantime, new cameras and telescopes are either being built or planned to offer much higher performance than we have achieved. We think that widening of the field of view is crucial for Suprime-Cam to remain competitive with such cameras in the future.

Acknowledgments

We are grateful to Prof. Katsuyuki Suzuki for his advice about the FEM simulation of the mechanical structure. We thank Wataru Kawasaki for his contribution in estimating the limiting magnitudes during the early phase of the project. We also appreciate Yasuhiro Sawada for his careful handcraft of wiring inside the dewar. Thanks are especially due to all of the staff members at Advanced Technology Center, National Astronomical Observatory for their help and support where Suprime-Cam was actually assembled and built.

Appendix 1. Effect of Atmospheric Differential Refraction

Atmospheric differential refraction affects various measurements in astronomy. In particular, it often sets the ultimate limitation on the field size we may hope to reach in wide-field imaging, such as Schmidt observations (Bowen 1967; Wallace & Tritton 1979; Filippenko 1982; Watson 1984, and references therein).

The field of view of the Subaru prime focus is much smaller than that of the typical Schmidt telescope. However, atmospheric differential refraction may have some effects, even over a 30' field of view of Suprime-Cam, due to the very good image quality. We simulate the effect based on the approximation formula derived by Tanaka (1993), which is valid at the summit of Mauna Kea.

Tanaka (1993) expressed the refractive index, n , of the atmosphere as $n = (1 + \rho)$, and compute ρ as follows. At the sea level (pressure $p = 760$ mmHg), dry atmosphere with 0.03% of CO₂ at the temperature $t = 15^\circ\text{C}$ have

$$\rho_2 \times 10^8 = 6432.8 + \frac{2949810}{146 - (1/\lambda)^2} + \frac{25540}{41 - (1/\lambda)^2}, \quad (\text{A1})$$

where λ is the wavelength in units of μm and the equation is valid for 0.2-1.35 μm . This value is corrected for lower temperature t ($^\circ\text{C}$) and lower pressure p (mmHg) at the summit as

Table 11. Characteristics of Suprime-Cam.

Prime Focus	Non-vignetted FOV	$30'\phi$ (13.5 cm ϕ)
	F-ratio	1.86
	Field curvature	negligible
	Atmospheric dispersion corrector	Lateral shift type
CCD	Type	MIT/LL CCID20
	Format	4096×2048 pixels
	Pixel size	15 μm (0."202)
	Number of CCDs	10 (2 \times 5)
	Quantum efficiency	400nm 55%
	(Typical)	600nm 80%
		800nm 89%
		1000nm 18%
	Operating temperature	-110°C
Cooler	Dark current	2-3 e hr ⁻¹ /pixel
	FOV covered by mosaic	34' \times 27'
Cooler	Type	Stirling cooler Daikin WE-5000
	Cooling capacity	5 W at 80 K, 16 W @163K
	Overhaul maintenance cycle	5000 h
Shutter	Minimum exposure time	1.2 s
Filter Filter exchanger	Physical dimension	205 mm \times 170 mm \times 15 mm
	Weight	1.3 kg
	Number of loadable filters	10
	Exchange time	5 min
Size	960 mm ϕ \times 1035 mm	
Weight	295 kg	
Power consumption	420 W (600 W max)	

$$\rho_1 = \rho_2 \times \frac{p_0[1 + (1.049 - 0.0157t) \times 10^{-6}p_0]}{720.883(1 + 0.003661t)}, \quad (\text{A2})$$

where

$$p_0 = p \times \frac{g}{g_0}, \quad (\text{A3})$$

where p is the measured pressure, g is the measured gravity, and $g_0 = 980.665$ gal is the standard gravity. The effect of water vapor can be corrected as

$$\rho_0 = \rho_1 - \frac{6.24 - 0.0680/\lambda^2}{1 + 0.003661t} \times f \times 10^{-8}, \quad (\text{A4})$$

with the pressure of water vapor f (mmHg). The atmospheric refraction can be computed by integrating the deflection angle of incoming light,

$$di = \tan i \, dn/n, \quad (\text{A5})$$

from the observer, where $n = n_0 = (1 + \rho_0)$, to the upper limit of the atmosphere.

Based on the model atmosphere for the set of parameter values typical at the summit of Mauna Kea (4180 m), that is, $p = 450$ mm Hg, $g = 978.627$ gal, $t = 0^\circ\text{C}$, and $f = 1$ mmHg, Tanaka (1993) obtained $\rho_0 = 0.00017352$ at $\lambda = 0.575 \, \mu\text{m}$, and derived the following approximation formula:

$$r = 35.''746 \tan z - 0.''0431 \tan^3 z + 0.''000164 \tan^5 z, \quad (\text{A6})$$

where r is the atmospheric refraction and z is the zenith distance. The differential refraction is also approximated as

$$dr/dz = 0.''624 \sec^2 z \, (\text{deg}^{-1}). \quad (\text{A7})$$

We assume that the guide star is at the field center, and compute the positions of 8 hypothetical stars projected onto the standard coordinate (ξ, η) on the focal plane. The offset from the optical axis (field center) of the eight stars are $\Delta\alpha/\cos\delta = 0', \pm 15'$ and $\Delta\delta = 0', \pm 15'$. The computation proceeds as follows. Assume that the celestial sphere is a unit sphere, and let the celestial North Pole and field center be $\vec{p} = (0, 0, 1)$ and $\vec{s}_c = (\cos\delta, 0, \sin\delta)$, respectively. Then, the zenith is expressed by

$$\vec{z} = (\cos h \cos \phi, \sin h \cos \phi, \sin \phi), \quad (\text{A8})$$

where h is the hour angle, and ϕ is the latitude of the observer. The zenith distance of the field center is given by

$$\cos z_c = \vec{s}_c \cdot \vec{z}. \quad (\text{A9})$$

This expression can be used to compute

$$\tan z_c = [1/\cos^2 z_c - 1]^{1/2}, \quad (\text{A10})$$

and then the atmospheric refraction r_c according to equation A6. Using the thus-computed r_c , the coordinates of the refracted field center are given by

$$\vec{s}'_c = \left(\cos r_c - \frac{\sin r_c}{\tan z_c} \right) \vec{s}_c + \frac{\sin r_c}{\sin z_c} \vec{z}. \quad (\text{A11})$$

Similarly, a star located off the field center by $(\Delta\alpha, \Delta\delta)$ with

$$\vec{s} = [\cos \Delta\alpha \cos(\delta + \Delta\delta), \sin \Delta\alpha \cos(\delta + \Delta\delta), \sin(\delta + \Delta\delta)] \quad (\text{A12})$$

is also refracted to

$$\vec{s}' = \left(\cos r - \frac{\sin r}{\tan z} \right) \vec{s} + \frac{\sin r}{\sin z} \vec{z}. \quad (\text{A13})$$

We then project \vec{s}' onto \vec{s}'_c using the North Pole vector, \vec{p} , to obtain

$$\xi = \frac{1}{\vec{s}' \cdot \vec{s}'_c} \frac{(\vec{s}'_c \times \vec{p})}{|\vec{s}'_c \times \vec{p}|} \cdot \vec{s}', \quad (\text{A14})$$

$$\eta = \frac{1}{\vec{s}' \cdot \vec{s}'_c} \frac{\vec{s}'_c \times (\vec{s}'_c \times \vec{p})}{|\vec{s}'_c \times \vec{p}|} \cdot \vec{s}' \quad (\text{A15})$$

Figure 23 shows the trail of 8 hypothetical stars around the field centers of $\delta_c = -30^\circ$, 0° , $+30^\circ$, and $+60^\circ$, respectively. The simulated exposure was 6 hr from hour-angle $h = -3^h$ to $h = +3^h$ with a dot at every 0.5 hour. Figure 24 shows the maximum exposure time during which the distortion of the stars at the edge of the Suprime-Cam field does not exceed $0.''1$. Computations were made for 12 fields centered between $\delta_c = +80^\circ$ and $\delta_c = -40^\circ$ with $\Delta\delta_c = 10^\circ$. For each field 13 exposures were simulated which start at hour angles between $h = -3^h$ and $h = +3^h$ with $\Delta h = 0.5$ hour. The abscissa was the $\sec z$ at the beginning of the exposure.

We make a few remarks based on this simulation. First, if we took $0.''1$ as the limit of distortion, the longest allowable exposure time was about 40 min at $z = 30^\circ$ and about 15 min at $z = 45^\circ$. It is noted, however, that a longer exposure could be made depending upon the location of the field. Second, even in the case we stacked many short exposure frames, image distortion could become a problem if individual exposures scatter in the wide range of the zenith distances. Finally, actual guiding was provided using a star near the edge of the field. The amount of the guiding which gave the best image at the field center could be computed by taking the effect of the differential refraction into account.

References

- Bessell, M. S. 1990, *PASP*, 102, 1181
 Boulade, O., Charlot, X, Abbon, P., Aune, S., Borgeaud, P., Carton, P.-H., Carty, M., Desforge, D., et al. 2000, *Proc. SPIE*, 4008, 657
 Blouke, M. M., Woody, T., Dosluoglu, T., Elliott, S. T., Janesick, J. R., Reed, R., & Stover, R. 1998, in *Optical Detectors for Astronomy*, ed. J.W. Beletic & P. Amico, (Dordrecht, Kluwer Academic Publisher), 3
 Bowen, I.S. 1967, *QJRAS*, 8, 9

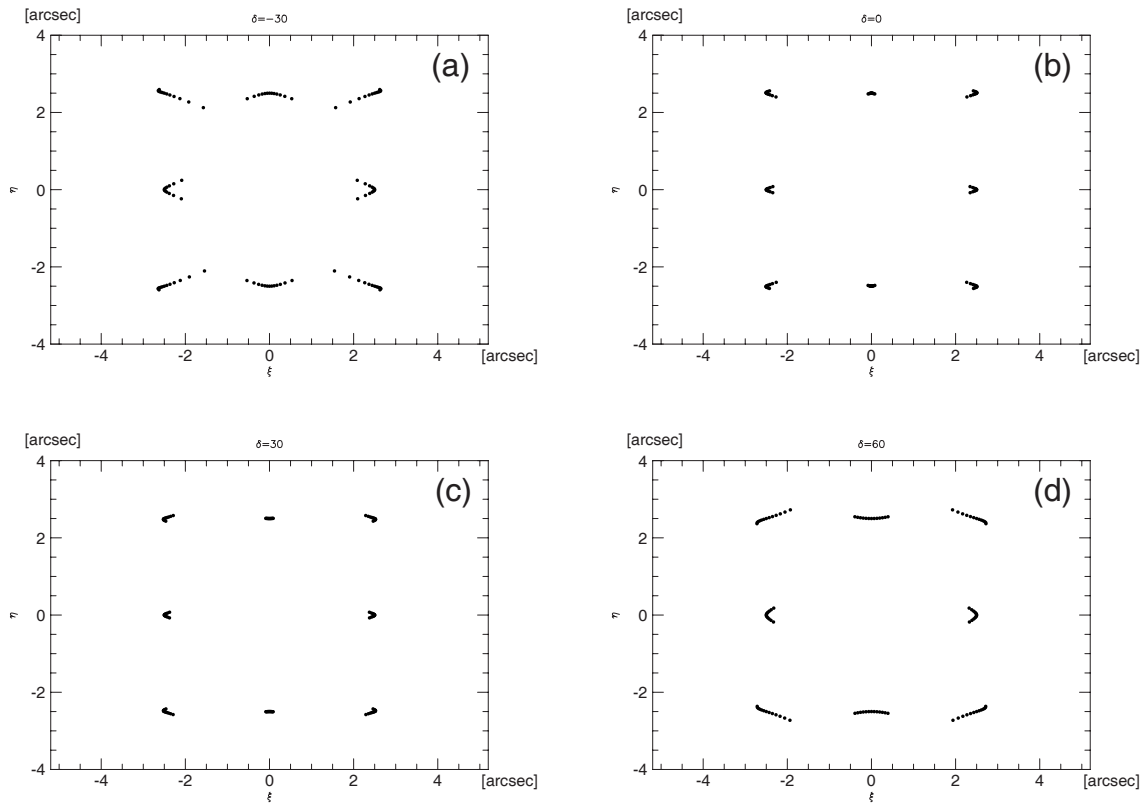


Fig. 23. Trails of eight hypothetical stars showing the effect of the atmospheric differential refraction for the fields centered at $\delta_c = -30^\circ$ (a), 0° (b), $+30^\circ$ (c), and 60° (d). The stars are placed at $d\xi = 0, \pm 15'$, and $d\eta = 0, \pm 15'$ from the field center, which correspond to the edge of the field of view of Suprime-Cam. The simulated exposure was 6 hr from hour angle $h = -3^h$ to $h = +3^h$ with a dot every 0.5 hour. North is up and the position of each trail is arbitrarily shifted so that the eight trails fit in one figure.

- Burke, B.E., Gregory, J.A., Mountain, R.W., Kosicki, B.B., Savoye, E.D., Daniels, P.J., Dolat, V.S., Lind, T.L., Loomis, A.H., Young, D.J., Luppino, G.A., & Tonry, J.L. 1998, in *Optical Detectors for Astronomy*, ed. J.W. Beletic & P. Amico, (Dordrecht: Kluwer Academic Publisher), 19
- Cavadore, C., Dorn, R.J., & Beletic, J.W. 2000, in *Optical Detectors for Astronomy II*, ed. P. Amico & J.W. Beletic, (Dordrecht: Kluwer Academic Publisher), 25
- Cousins, A. W. J. 1978, *Mon. Notes Astron. Soc. S. Afr.*, 37, 8
- Cowie, L.L, & Hu, E. M. 1998, *AJ*, 115, 1319
- Filippenko, A.V. 1982, *PASP*, 94, 715
- Fukugita, M., Shimasaku, K., & Ichikawa, T. 1995, *PASP*, 107, 945
- Fukugita, M., Ichikawa, T., Gunn, J. E., Doi, M., Shimasaku, K., & Schneider, D. P. 1996, *AJ*, 111, 1748
- Greisen, E. W. & Calabretta, M. 2002 in preparation
- Gunn, J.E., & Weinberg, D. 1995, in *Wide Field Spectroscopy and the Distant Universe*, eds. S.J.Maddox & A.Aragon-Salamanca (Singapore: World Scientific), 3
- Gunn, J. E., Carr, M., Rochosi, C., Sekiguchi, M., Berry, K., Elms, B., de Haas, E., Ivezić, Z., et al.

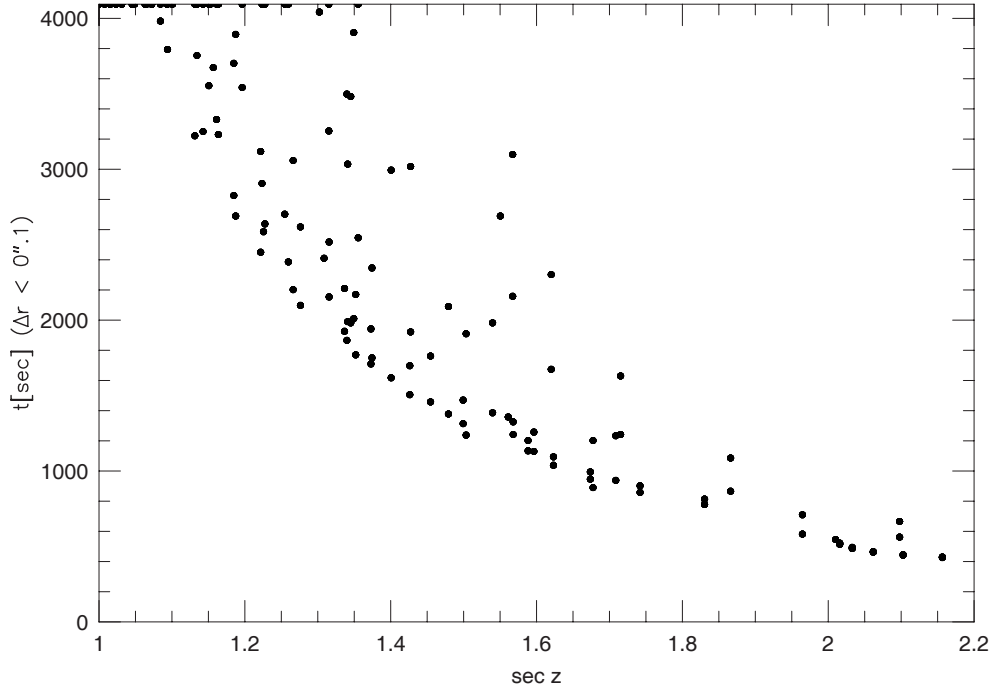


Fig. 24. Maximum exposure time plotted as a function of the air mass ($\sec z$) at the beginning of an exposure. The maximum exposure time is defined as the time during which the distortion of stars at the edge of the Suprime-Cam field does not exceed $0''.1$. Computations were made for 12 fields centered between $\delta_c = +80^\circ$ and $\delta_c = -40^\circ$ with $\Delta\delta_c = 10^\circ$. For each field 13 exposures were simulated, which start at hour angles of between $h = -3^h$ and $h = +3^h$ with $\Delta h = 0.5$ hour.

1998, AJ, 116, 3040

Johnson, H. L., & Morgan, W. W. 1953, ApJ, 117, 313

Kaiser, N., Squires, G., & Broadhurst, T. 1995, ApJ, 449, 460

Kaier, N. 2002, Proc. SPIE, 4836 in press

Kosugi, G., Sasaki, T., Aoki, T., Kawai, J. A., Koura, N., & Kusumoto, T. 1997, Proc. SPIE, 3112, 284

Lifshitz, E. M., & Landau, L. D. 1953, Theory of elasticity, Course of theoretical physics, vol 7, (London: Pergamon Press)

Luppino, G. A., & Miller, K. R. 1992, PASP, 104, 215

McClure, R. D., Grundmann, W. A., Rambold, W. N., Fletcher, J. M., Richardson, E. H., Stillburn, J. R., Racine, R., Christian, C. A. & Waddell, P. 1989 PASP, 101, 1156

Nakata, F., Miyazaki, S., Okada, N., Kimura, M., & Sekiguchi, M. in Optical Detectors for Astronomy II, ed. P. Amico & J.W. Beletic, (Dordrecht: Kluwer Academic Publisher), 133

Nariai, K., & Takeshi, K. 1994, Proc. SPIE, 2199, 532

- Nariai, K., Yamashita, Y., & Nakagiri, M. 1985, *Ann. Tokyo Astron. Obs.*, 2nd Series, 20, 431
- Oates, A. P., & Jorden, P. R. 1998, in *Optical Detectors for Astronomy*, ed. J.W. Beletic & P. Amico, (Dordrecht: Kluwer Academic Publisher) ,143
- Perlmutter, S., Gavi, S., Gddhaber, G., Gooban, A., Groom, D.E., Hook, I.M, Kim, A.G., Kim, M.Y., et al. 1997, *ApJ*, 483, 565
- Sasaki, T., Kosugi, G., Noumaru, J., Takata, T., Mizumoto, Y., Ogasawara, R., Chikada, Y., Tanaka, W., & Kawai, J. A. 1998, *Proc. SPIE*, 3349, 427
- Sekiguchi, M., Nakaya, H., Kataza, H., & Miyazaki, S. 1998, in *Optical Detectors for Astronomy*, ed. J.W. Beletic & P. Amico, (Dordrecht: Kluwer Academic Publisher) ,157
- Steidel, C.C., Giavalisco, M., Pettini, M., Dickinson, M., Adelberger, K. L. 1996, *ApJL*, 462, L17
- Takata, T., Ogasawara, R., Kosugi, G., Mizumoto, Y., Ichikawa, S., Yasuda, N., Taga, M., Yagi, M., et al. 2000, *Proc. SPIE*, 4010, 181
- Takeshi, K., 2000, PhD Thesis, The graduate university for advanced studies
- Tanaka, W. 1993, Report of National Astron. Obs. Japan, 1, 349 (in Japanese)
- Tonry, J.L, Luppino, G.A., Kaiser, N., Burke, B., & Jacoby, G. 2002, *Proc. SPIE*, 4836, in press
- Tyson, J.A., Wenk, R.A., & Valdes, F. 1990, *ApJL*, 349, L1
- Tyson, A. & Angel, R. 2001, in *ASP Conf. Ser.*, 232 347
- van Waerbeke, L., Mellier, Y., Erben, T., Cuillandre, J. C., Bernardeau, F., Maoli, R., Bertin, E., Mc Cracken, et al. 2000, *A&A*, 358, 30
- Wallace, P.T., & Tritton, K.P. 1979, *MNRAS*, 189, 115
- Watson, F.G. 1984, *MNRAS*, 206, 661
- Wei, M., & Stover, R.J. 1998, *Proc. SPIE*, 3355, 598
- Williams, R.E., Blacker, B., Dickinson, M., Dixon, W. van Dyke, Feerguson, H.C., Fruchter, A.S., Giavalisco, M., Gilliland, R.L., Heyer, I., et al. 1996, *AJ*, 112, 1335
- Wolfe, T., Reed, R., Blouke, M.M., Boroson, T.A., Armandroff, T., & Jacoby, G.H. 1998, *Proc. SPIE*, 3355, 487
- Wynne, C.G. 1965, *Appl. Opt.*, 4, 1185